

Time-Varying Multi-Seasonal AR Models

Ganna Fagerberg^{a*}, Mattias Villani^a and Robert Kohn^{b,c}

We propose a seasonal AR model with time-varying parameter processes in both the regular and seasonal parameters. The model is parameterized to guarantee stability at every time point and can accommodate multiple seasonal periods. The time evolution is modeled by dynamic shrinkage processes to allow for long periods of essentially constant parameters, periods of rapid change as well as abrupt jumps. A Gibbs sampler is developed with a particle Gibbs update step for the AR parameter trajectories. The near-degeneracy of the model, caused by the dynamic shrinkage processes, is shown to pose a challenge for particle methods. To address this, a more robust, faster and accurate approximate sampler based on the extended Kalman filter is proposed. The model and the numerical effectiveness of the Gibbs sampler are investigated on simulated and real data. An application to more than a century of monthly US industrial production data shows interesting clear changes in seasonality over time, particularly during the Great Depression and the recent Covid-19 pandemic.

Keywords: Bayesian inference; Extended Kalman filter; Locally stationary processes; Particle MCMC; Seasonality.

1 Introduction

Autoregressive integrated moving average (ARIMA) models, originally popularized in the seminal book by Box and Jenkins (1970), form a parsimonious and versatile class of time series models. ARIMA models have proven invaluable for analyzing time series data, particularly the subclass of AR models. Their parsimony is even more apparent when modeling seasonality with the elegant multiplicative structure in ARIMA models. Importantly, this structure directly extends to models with multiple seasonal periods, an increasingly common feature in time series data.

A drawback of the Box-Jenkins methodology is the requirement of stationarity, i.e. that the process exhibits constant statistical properties over time, or can be differenced

*Corresponding author: ganna.fagerberg@stat.su.se. ^aDepartment of Statistics, Stockholm University.

^bSchool of Business, University of New South Wales. ^cData Analytics Center for Resources and Environments (DARE).

to stationarity. Time series data are often recorded over long study periods, and/or at high-frequency in rapidly changing environments. The statistical characteristics of such time series are likely to undergo substantial changes, which may occur both gradually and suddenly. These may be due to inherent process dynamics or external factors like pandemics, wars, and natural disasters. The common recommendation to difference the series to achieve stationarity can lead to over-differencing, resulting in misleading inferences (Granger and Joyeux, 1980) and poor forecasts (Makridakis and Hibon, 1997; Smith and Yadav, 1994). Using data only from the most recent regime is wasteful since many correlations are expected to survive regime shifts. Moreover, this approach prevents the model from assigning any probability to future regime changes.

A more flexible approach assumes local stationarity where the process is stationary over shorter time segments, or stationary in a small neighborhood around each time point, see e.g. Dahlhaus (2000) for a theoretical framework. This allows for a flexible modeling framework capable of accommodating dynamic changes in key attributes of the process. One strand of literature explicitly models a small set of stationary regimes, with abrupt jumps between regimes, see e.g. the Markov switching type of models in Hamilton (1989) or change-point models in Chib (1998) and Rosen et al. (2012), and dynamic mixture models in Gerlach et al. (2000). Another popular approach that has found widespread applications across various fields is the class of time-varying autoregressive (TVAR) models (Prado and West, 2010; Yang et al., 2014; Lubik and Matthes, 2015; Wood et al., 2011). The parameters in TVAR models evolve more gradually over time following a stochastic process, typically a random walk with Gaussian innovations. The TVAR models with Gaussian parameter evolution have also been extended to the multivariate case (Doan et al., 1984; Primiceri, 2005). More recently, there has been progress in more realistic models for the parameter evolution that use local-global shrinkage priors (Carvalho et al., 2010) to cater for smooth gradual changes, periods with no change, as well as abrupt jumps, see e.g. Kalli and Griffin (2014), Kowal et al. (2019), Cadonna et al. (2020) and Knaus and Frühwirth-Schnatter (2023).

In AR models with static parameters, it is common to parameterize the AR coefficients to guarantee stability/stationarity. Barndorff-Nielsen and Schou (1973) and Monahan (1984) define a recursion from unrestricted parameters via the partial autocorrelations to the AR parameters in the stable/stationary region. However, stability restrictions are rarely imposed in the time-varying parameter AR models (Everitt et al. (2013) , Godsill et al. (2004) and Yang et al. (2014) are exceptions with models for time-varying partial autocorrelations). A process with time-varying parameters may however easily drift into the non-stable regions for certain time periods leading to unwanted explosive forecast paths. The main reason for not imposing stability in time-varying models is most likely computational: the stability restrictions are non-linear and the Kalman filter can therefore no longer be used for inference. The same is true for the forward-filtering backward sampling (FFBS) algorithm (Carter and Kohn, 1994; Frühwirth-Schnatter, 1994) which uses the Kalman filter as a key component.

Seasonality is a neglected aspect of time-varying models, and all of the aforementioned articles deseasonalize the data before the analysis. The regularities provided by seasonality

are perhaps the most predictable pattern in a time series and there is much to gain from modeling time-varying seasonality jointly with other model parameters. The absence of time-varying seasonality within the ARIMA framework is probably due to the non-linearity resulting from the multiplicative seasonal structure, again precluding the use of the Kalman filter for inference. This is unfortunate, since the multiplicative seasonal AR representation in Box et al. (2015) directly extends to multiple seasonal patterns, which are an increasingly common feature in many datasets; for example, hourly measurements can exhibit daily, weekly and annual cycles (Xie and Ding, 2020; De Livera et al., 2011).

Our article makes the following contributions. First, a time-varying seasonal AR process is developed where both the regular and the seasonal AR parameters follow the dynamic shrinkage process priors in Kowal et al. (2019). The proposed model is shown to effectively track evolving patterns in parameter values over time, including jumps, while accurately identifying periods of constant parameters. Second, the model is extended to the case with multiple seasonal periods. Third, we explicitly restrict the parameters to a stable process at every time point using the parameterization in Barndorff-Nielsen and Schou (1973) and Monahan (1984), ensuring that the process is locally stable. Finally, Gibbs sampling algorithms are developed to handle the nonlinearities in the time-varying parameters stemming from both the multiplicative seasonality and stability restrictions.

We propose a fully Bayesian approach to jointly estimate the time-varying seasonal and non-seasonal AR coefficients of the seasonal TVAR model. We develop a Gibbs sampling algorithm to deal with the non-linearity in the multiplicative seasonal structure and the stability restriction. The algorithm updates the regular and seasonal AR parameters using the particle Gibbs with ancestor sampling (PGAS, Lindsten et al. (2014)) algorithm. While this sampler is simulation consistent, it is relatively time-consuming and may suffer from degeneracy due to the dynamic shrinkage prior, which encourages parameter paths to remain essentially constant over extended time periods. Therefore, we develop an alternative updating step using the forward-filtering backward sampling (FFBS) algorithm (Carter and Kohn, 1994; Frühwirth-Schnatter, 1994), with the filtering step performed by the extended Kalman filter (Thrun et al., 2005) to handle the two types of non-linearities in the model. The extended Kalman filter is an approximate filter, but we demonstrate that it is quite accurate in seasonal AR models with stability restrictions.

We explore the properties of the proposed model and posterior sampling algorithms in several simulation experiments. The model is shown to compare favorably to several widely used time-varying parameter models. Finally, the model is applied to more than a century of monthly industrial production data in the US. We find strong evidence of time-varying parameters, particularly in the seasonal AR parameters, where the otherwise strong seasonality is essentially wiped out during the Great Depression, and is also markedly different during the Covid-19 pandemic.

The proofs and additional results are available in the supplementary material to this article, referenced below with the prefix S, e.g. Figure S1 in Section S1.

2 Time-varying AR processes with multiple seasonal periods

2.1 Multi-seasonal AR processes

We start by introducing the static, or time invariant, stationary multi-seasonal AR model (SAR) and then extend the model to the time-varying parameter case. A general AR model that encompasses one or more seasonal components is expressed as (Wei, 2019)

$$\prod_{j=1}^M \phi_j(L^{s_j})(y_t - m) = \varepsilon_t, \quad (2.1)$$

where m is the mean, L is the usual lag operator with the property $L^k y_t = y_{t-k}$ and $\varepsilon_t \stackrel{\text{iid}}{\sim} N(0, \sigma^2)$ is a white noise sequence. The factor $\phi_j(L^{s_j}) = 1 - \phi_{j1}L^{s_j} - \phi_{j2}L^{2s_j} - \dots - \phi_{jp_j}L^{p_j s_j}$ is a polynomial in the lag operator L for the j^{th} AR component with seasonal period s_j , with M being the total number of components. We denote this model by SAR(\mathbf{s}, \mathbf{p}), where $\mathbf{s} = (s_1, \dots, s_M)$ is a vector with the seasonal periods for the components and $\mathbf{p} = (p_1, \dots, p_M)$ are the corresponding lag orders for each seasonal component.

The model in (2.1) is highly flexible and accommodates both purely non-seasonal processes as well as combinations of non-seasonal and seasonal processes with multiple seasonal periods. For example, when $M = 1$ and $s_1 = 1$, the model reduces to a pure AR model without seasonality. When $M = 2$ with one regular ($s_1 = 1$) and one seasonal polynomial with season s ($s_2 = s$), we obtain the standard single season AR model

$$\phi(L)\Phi(L^s)(y_t - m) = \varepsilon_t, \quad (2.2)$$

where $\phi(L) = 1 - \phi_1 L - \dots - \phi_p L^p$ and $\Phi(L) = 1 - \Phi_1 L^s - \dots - \Phi_P L^{Ps}$, using the traditional notation with capital letters for the seasonal AR parameters. For models with a single seasonal period with a given seasonal period s we will write SAR(p, P) as a shorthand for SAR($\mathbf{s} = (1, s), \mathbf{p} = (p, P)$).

As an example of a model with both a regular and multiple seasonal components, consider a model for daily data with $M = 3$ and $\mathbf{s} = (1, 7, 30)$, so that the model is a SAR model with both a weekly ($s_2 = 7$) and a monthly cycle ($s_3 = 30$)

$$\phi_1(L)\phi_2(L^7)\phi_3(L^{30})(y_t - m) = \varepsilon_t,$$

where $\phi_1(L) = 1 - \phi_{11}L - \dots - \phi_{1p_1}L^{p_1}$ is the regular AR polynomial while $\phi_2(L^7) = 1 - \phi_{21}L^7 - \dots - \phi_{2p_2}L^{7p_2}$ and $\phi_3(L^{30}) = 1 - \phi_{31}L^{30} - \dots - \phi_{3p_3}L^{30p_3}$ are the two seasonal AR polynomials.

The SAR(\mathbf{s}, \mathbf{p}) process in (2.1) is stable if all lag polynomials $\phi_j(L^{s_j})$ are such that $|\phi_j(z)| \neq 0$, for $|z| \leq 1$. A stable process has many desirable properties, e.g. non-explosive forecast paths, existence of a spectral density, and well-behaved impulse response functions. A stable process is also stationary. The model in (2.1) can also include polynomials that apply regular differencing $\phi_j(L) = 1 - L$ or seasonal differencing $\phi_j(L^{s_j}) = 1 - L^{s_j}$. Such unit root polynomials can always be added in our approach,

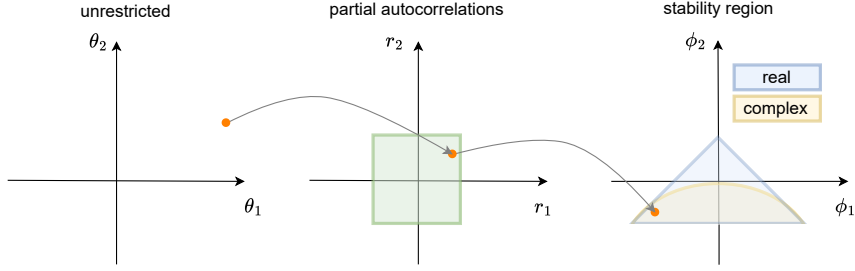


Figure 1: Illustrating the stability parametrization from an AR(2) process from the unrestricted $\boldsymbol{\theta} = (\theta_1, \theta_2)^\top \in \mathbb{R}^2$ (left) via the partial autocorrelations $\mathbf{r} = (r_1, r_2)^\top \in (-1, 1)^2$ (middle) to the AR parameters $\boldsymbol{\phi} = (\phi_1, \phi_2)^\top$ (right); the regions with real (blue) and complex (beige) roots are also shown.

and the given stability conditions for the remaining polynomial factors then guarantee stability for the differenced or seasonally differenced series. Since the stability restrictions imply the same set of restrictions on the $\boldsymbol{\phi}$ parameters in each polynomial, we now restrict attention to the regular AR polynomial $\phi(L) = 1 - \phi_1 L - \dots - \phi_p L^p$, and drop all subscripts referring to the individual polynomial terms.

To enforce stability we use the reparametrisation in Barndorff-Nielsen and Schou (1973) and Monahan (1984) to map a set of unconstrained real-valued coefficients to the set of stable parameters, i.e. parameters that determine a stable process. Let $\mathbb{S}^p \subset \mathbb{R}^p$ denote the region in parameter space where the AR(p) process is stable. The reparameterization is defined as follows.

Definition 1 (stability parameterization). *An AR(p) process can be restricted to be stable by a 1:1 and onto map*

$$\boldsymbol{\theta} \rightarrow \mathbf{r} \rightarrow \boldsymbol{\phi}.$$

of unrestricted parameters $\boldsymbol{\theta} = (\theta_1, \dots, \theta_p)^\top \in \mathbb{R}^p$ via the partial autocorrelations $\mathbf{r} = (r_1, \dots, r_p)^\top \in (-1, 1)^p$ to the stable AR parameters $\boldsymbol{\phi} = (\phi_1, \dots, \phi_p)^\top \in \mathbb{S}^p$. The mapping from \mathbf{r} to $\boldsymbol{\phi}$ is given by setting $\phi_{1,1} = r_1$ followed by the recursion

$$\phi_{k,j} = \phi_{k-1,j} + r_k \phi_{k-1,k-j}, \quad \text{for } k = 2, \dots, p \text{ and } j = 1, \dots, k-1,$$

and final returning $\boldsymbol{\phi} = (\phi_{p,1}, \dots, \phi_{p,p})^\top$, where $\phi_{p,p} = r_p$.

Definition 1 leaves open the choice of transformation from the unrestricted parameters to the partial correlations, $\boldsymbol{\theta} \rightarrow \mathbf{r}$. We use the transformation suggested by Monahan (1984)

$$r_k = \frac{\theta_k}{\sqrt{1 + \theta_k^2}} \quad \text{for } k = 1, \dots, p. \quad (2.3)$$

Figure 1 illustrates the two mappings involved in the parametrization.

The unrestricted parameters $\boldsymbol{\theta} = (\theta_1, \dots, \theta_p)^\top$ in (2.3) are merely technical devices and are not interpretable. The following lemma gives the prior on $\boldsymbol{\theta}$ which implies a uniform distribution over the stable/stationary region for the AR parameters; its proof is in Section S1.1. A uniform distribution can be used as a baseline for more informative distributions.

Lemma 1. *Let $\boldsymbol{\phi} = \mathbf{g}(\boldsymbol{\theta})$ be the mapping in Definition 1, and let $\theta_1, \dots, \theta_p$ be independently distributed as*

$$\theta_k \sim \begin{cases} t(k+1, 0, \frac{1}{\sqrt{k+1}}) & \text{if } k \text{ is odd} \\ t_{\text{skew}}(\frac{k}{2}, \frac{k+2}{2}, 0, \frac{1}{\sqrt{k+1}}) & \text{if } k \text{ is even,} \end{cases} \quad (2.4)$$

then $\boldsymbol{\phi} = \mathbf{g}(\boldsymbol{\theta})$ is uniform over the stability region in $\boldsymbol{\phi}$ -space. Here $t(v, \mu, \sigma)$ is the usual t -distribution with v degrees of freedom translated by μ and scaled by σ , and $t_{\text{skew}}(a, b, \mu, \sigma)$ is the skew- t extension in Jones and Faddy (2003).

2.2 Locally stable time-varying multi-seasonal AR processes

The dynamic, or time-varying, AR model with multiple seasonal components

$$\prod_{j=1}^M \phi_{jt}(L^{s_j})y_t = \varepsilon_t, \quad \varepsilon_t \sim N(0, \sigma^2) \quad (2.5)$$

extends the model in (2.1) with time-varying AR polynomials

$$\phi_{jt}(L^{s_j}) = 1 - \phi_{j1t}L^{s_j} - \phi_{j2t}L^{2s_j} - \dots - \phi_{jp_jt}L^{p_j s_j}.$$

The errors ε_t can be generalized to have time-varying noise variance, see Section S3.5 and the empirical application in Section 5. We also assume that the process has a zero mean, but a non-zero time-varying mean m_t can be included in the model. We denote this model by TVSAR(\mathbf{s}, \mathbf{p}), where, as before, $\mathbf{s} = (s_1, \dots, s_M)$ is a vector with the M seasonal periods and $\mathbf{p} = (p_1, \dots, p_M)$ are the corresponding lag orders.

Time-varying parameter models run the risk of drifting into the non-stable region with explosive behavior during certain time periods, resulting in erratic predictions; see Godsill et al. (2004) for a discussion in the context of speech data analysis. We therefore assume that all polynomials in model (2.5) satisfy the stability conditions at every time period t . Note that this is an assumption of *local* stability; we do not impose the restrictive assumption of global stationarity with constant parameters as in the Box-Jenkins methodology. To enforce local stability in the dynamic AR process, we employ the parameterization described in Definition 1. At each time period t , we map the unrestricted time-varying parameters $\boldsymbol{\theta}_t = (\theta_{1t}, \dots, \theta_{pt})^\top$ to the time-varying AR parameters $\boldsymbol{\phi}_t = (\phi_{1t}, \dots, \phi_{pt})^\top$. This restriction is imposed on each AR polynomial in (2.5), but we suppress the polynomial index for notational clarity.

The unrestricted parameters $\boldsymbol{\theta}_t$ evolve over time following the dynamic shrinkage process (DSP) recently developed in Kowal et al. (2019). The dynamic shrinkage process

is a time series extension of the widely used horseshoe prior (Carvalho et al., 2010), allowing the parameters to be essentially unchanged for long periods followed by large jumps or potentially persistent periods of rapid change. The process for the evolving TVSAR parameters in any given AR polynomial with p lags is

$$\begin{aligned}\phi_t &= \mathbf{g}(\boldsymbol{\theta}_t) \\ \theta_{kt} &= \theta_{k,t-1} + \nu_{kt}, & \nu_{kt} &\stackrel{\text{indep}}{\sim} N(0, \exp(h_{kt})) \\ h_{kt} &= \mu_k + \kappa_k(h_{k,t-1} - \mu_k) + \eta_{kt}, & \eta_{kt} &\stackrel{\text{iid}}{\sim} Z(1/2, 1/2, 0, 1),\end{aligned}\quad (2.6)$$

for $k = 1, \dots, p$, where $\phi_t = \mathbf{g}(\boldsymbol{\theta}_t)$ maps the unrestricted parameters $\boldsymbol{\theta}_t \in \mathbb{R}^p$ to the stable parameters $\phi_t \in \mathbb{S}^p$. The global mean log-volatilities $\boldsymbol{\mu} = (\mu_1, \dots, \mu_p)^\top$ control the overall degree of time-variation in $\boldsymbol{\theta}_t$ and consequently in ϕ_t . The parameter κ_k regulates the persistence of the log-volatility process h_{kt} for the k th parameter. The innovations to the log-volatility are drawn from the heavy-tailed Z -distribution (Barndorff-Nielsen et al., 1982) with zero location and unit scale parameters. It is straightforward to add a scale parameter σ_η to $\eta_{kt} \sim Z(1/2, 1/2, 0, \sigma_\eta)$, but we have not found it necessary in our model.

The global log-volatilities μ_{kt} are modulated by the heavy-tailed local log-volatilities $\eta_{kt} \stackrel{\text{iid}}{\sim} Z(1/2, 1/2, 0, 1)$. A small global μ_k gives a prior with long periods of essentially constant evolution in θ_k . When a positive local heavy-tailed η_{kt} innovation occurs, it causes the log-volatility to temporarily spike and remain high for a duration governed by the persistence parameter κ_k . To see the connection to the original horseshoe prior in Carvalho et al. (2010), consider the case with no persistence, $\kappa_k = 0$. The variance of the innovations to the k th parameter is then $\exp(h_{kt}) = \tau_k^2 \lambda_{kt}^2$, where $\tau_k^2 = \exp(\mu_k)$ is the global variance and $\lambda_{kt}^2 = \exp(\eta_{kt})$ is the time-varying local variance. The implied prior on each λ_{kt} is $C^+(0, 1)$, i.e. a heavy tailed half-Cauchy as in the original horseshoe prior. Kowal et al. (2019) demonstrate that the DSP prior maintains the shrinkage characteristics of the original horseshoe prior when $0 < \kappa < 1$, with additional shrinkage in a time period that follows a period of heavy shrinkage. For a comprehensive treatment of the DSP process, see Kowal et al. (2019).

The prior for $\boldsymbol{\theta}_0$ is given by Lemma 2.4, implying a uniform distribution over the stability region. The log-volatilities at time $t = 0$ are given by $\mathbf{h}_0 = \boldsymbol{\mu} + \boldsymbol{\eta}_0$ with the elements of $\boldsymbol{\eta}_0$ independent $Z \sim (1/2, 1/2, 0, 1)$ a priori. The prior for each $\kappa_k \sim TN(\kappa_0, \psi_0^2, -1, 1)$ is a normal truncated to $(-1, 1)$. Kowal et al. (2019) use a Pólya-Gamma construction for the prior on the global means μ_k to obtain the original $C^+(0, 1)$ horseshoe prior for $\tau_k = \exp(\mu_k/2)$. This choice for the horseshoe prior is questioned by Piironen and Vehtari (2017) and we use $\mu_k \sim N(\mu_0, \sigma_0^2)$, implying a log normal prior for τ_k .

2.3 Conditional likelihood function for the time-varying multi-seasonal AR

The multi-seasonal TVSAR(\mathbf{s}, \mathbf{p}) model in (2.5) can be written as a single AR polynomial model by multiplying out the M AR polynomials $\prod_{j=1}^M \phi_{jt}(L^{s_j}) = \tilde{\phi}_t(L)$ and moving all

lags to the right hand side to obtain the regression model

$$y_t = \mathbf{x}_t^\top \tilde{\boldsymbol{\phi}}_t + \varepsilon_t, \quad \varepsilon_t \stackrel{\text{iid}}{\sim} N(0, \sigma^2), \quad (2.7)$$

where \mathbf{x}_t is a vector containing all lags y_{t-k} for which the coefficients in $\tilde{\boldsymbol{\phi}}_t(L)$ are non-zero and the vector $\tilde{\boldsymbol{\phi}}_t$ collects the coefficients for those lags. The elements of $\tilde{\boldsymbol{\phi}}_t$ are products of the AR parameters in the different polynomials. For example, consider a model with a regular component ($s_1 = 1$) with one lag and one seasonal component with period $s_2 = s$ and one lag

$$(1 - \phi_{1t}L)(1 - \Phi_{1t}L^s)y_t = \varepsilon_t, \quad (2.8)$$

using the notation with capital letters for seasonal coefficients and lag length P . Multiplying out the two polynomials on the left hand side of (2.8) and rearranging, the model can be written

$$y_t = \phi_{1t}y_{t-1} + \Phi_{1t}y_{t-s} - \phi_{1t}\Phi_{1t}y_{t-(1+s)} + \varepsilon_t, \quad (2.9)$$

so $\mathbf{x}_t = (y_{t-1}, y_{t-s}, y_{t-(1+s)})^\top$ and $\tilde{\boldsymbol{\phi}}_t = (\phi_{1t}, \Phi_{1t}, \phi_{1t}\Phi_{1t})^\top$ in (2.7). The three-dimensional vector of regression coefficients $\tilde{\boldsymbol{\phi}}_t$ is a nonlinear transformation of the two unrestricted AR parameters at time t . A general TVSAR model with M polynomials is a nonlinear transformation with a total of $r = \sum_{j=1}^M p_j$ unrestricted time-varying AR parameters.

We use the conditional likelihood function of the seasonal AR model based on the regression formulation in (2.7), conditional on p_{\max} pre-sample values $y_0, y_{-1}, \dots, y_{-p_{\max}+1}$ where p_{\max} is the maximal lag order in \mathbf{x}_t . Conditioning on pre-sample observations is typically unproblematic in purely regular AR models or seasonal models for quarterly or monthly data when working with sufficiently long datasets. For seasonal data observed at high frequency, this assumption can lead to a substantial information loss as the number of lost initial observations quickly becomes large for hourly or higher frequency data. An alternative approach is to use the exact likelihood (Hamilton, 2020) to avoid the loss of initial data. However, this is computationally costly, particularly in AR models with multiple seasonalities, and we leave this to future work.

In summary, the seasonal AR model with dynamic shrinkage priors is

$$\begin{aligned} y_t &= \mathbf{x}_t^\top \tilde{\boldsymbol{g}}(\boldsymbol{\theta}_t) + \varepsilon_t, & \varepsilon_t &\stackrel{\text{iid}}{\sim} N(0, \sigma^2) \\ \boldsymbol{\theta}_t &= \boldsymbol{\theta}_{t-1} + \boldsymbol{\nu}_t, & \boldsymbol{\nu}_t &\stackrel{\text{indep}}{\sim} N(\mathbf{0}, \text{Diag}(\exp(\mathbf{h}_t))) \\ \mathbf{h}_t &= \boldsymbol{\mu} + \boldsymbol{\kappa}(\mathbf{h}_{t-1} - \boldsymbol{\mu}) + \boldsymbol{\eta}_t, & \eta_{kt} &\stackrel{\text{iid}}{\sim} Z(1/2, 1/2, 0, 1), \end{aligned} \quad (2.10)$$

where $\boldsymbol{\theta}_t$ is a vector with all $r = \sum_{j=1}^M p_j$ AR coefficients and $\tilde{\boldsymbol{\phi}}_t = \tilde{\boldsymbol{g}}(\boldsymbol{\theta}_t)$ maps the coefficients in each AR polynomial to the stability region followed by the polynomial multiplication leading to $\tilde{\boldsymbol{\phi}}_t$ in (2.7). The $r \times r$ matrix $\boldsymbol{\kappa}$ is diagonal with $(\kappa_1, \dots, \kappa_r)^\top$ on its main diagonal and $\text{Diag}(\exp(\mathbf{h}_t))$ has $\exp(\mathbf{h}_t) = (\exp(h_{1t}), \dots, \exp(h_{rt}))^\top$ on its main diagonal.

3 Bayesian inference for time-varying seasonal AR

The joint posterior distribution for all unknown parameters $p(\boldsymbol{\theta}_{0:T}, \mathbf{h}_{0:T}, \sigma_{1:T}, \boldsymbol{\mu}, \boldsymbol{\kappa} | y_{1:T})$ is intractable. We sample from this posterior using Algorithm 1, which is a block Gibbs sampler, with each of the above parameter vectors as separate updating blocks. The notation $\boldsymbol{\theta}_{0:T}$ means the sequence of all r unrestricted AR parameters $\boldsymbol{\theta}_t$ for $t = 0, 1, \dots, T$.

We now explain the updating steps for $\mathbf{h}_{0:T}$ and $\boldsymbol{\theta}_{0:T}$, with the details of the updating steps for $\boldsymbol{\mu}$ and $\boldsymbol{\kappa}$ in Section S3; the updating steps for $\boldsymbol{\mu}$ and $\boldsymbol{\kappa}$ are slightly different from the ones in Kowal et al. (2019) due to different priors. The updating step for $\mathbf{h}_{0:T}$ is identical to that in Kowal et al. (2019), but is reviewed here as it explains the two data augmentation steps in the Gibbs sampler in Algorithm 1: the mixture allocation $\mathbf{a}_{1:T}$ and the Pólya-Gamma variables $\boldsymbol{\xi}_{0:T}$ for the Z -distribution.

3.1 Updating the log volatility paths

Conditional on the static parameters $\boldsymbol{\mu}$ and $\boldsymbol{\kappa}$ and the parameter paths $\boldsymbol{\theta}_{0:T}$, the sampling step for stochastic volatility models in Rue (2001) and Kastner and Frühwirth-Schnatter (2014) can be used to efficiently sample the r columns of $\mathbf{h}_{0:T}$ independently from multivariate normal distributions with a tri-diagonal covariance matrix. Since the log-volatilities for different parameters are drawn independently, we focus on one parameter and drop the subscript k and write h_t for the rest of this subsection.

The sampling of $h_{0:T}$ in Kowal et al. (2019) follows the log-volatility estimation in Kim et al. (1998) where the model for the parameter innovations $\nu_t = \theta_t - \theta_{t-1}$

$$\nu_t = \exp(h_t/2)\epsilon_t, \quad \epsilon_t \stackrel{\text{iid}}{\sim} N(0, 1) \quad (3.1)$$

is rewritten by squaring and taking logs on both sides

$$\log \nu_t^2 = h_t + \log \epsilon_t^2, \quad (3.2)$$

so that h_t becomes an additive term. The error term $\log \epsilon_t^2$ is however $\log \chi_1^2$ -distributed, which Kim et al. (1998) solves by approximating the $\log \chi_1^2$ distribution with a mixture of normals, thereby turning the model into a Gaussian model conditional on latent mixture allocation variables $\mathbf{a}_{1:T}$; we use the 10-component mixture in Omori et al. (2007).

The prior for the log-volatility $h_{0:T}$ series follows the dynamic shrinkage process

$$h_t = \mu + \kappa(h_{t-1} - \mu) + \eta_t, \quad \eta_t \stackrel{\text{iid}}{\sim} Z(1/2, 1/2, 0, 1), \text{ for } t = 1, \dots, T, \quad (3.3)$$

with initial condition $h_0 = \mu + \eta_0$ and $\eta_0 \sim Z(1/2, 1/2, 0, 1)$. Kowal et al. (2019) show that the prior can be augmented with Pólya-Gamma variables $\boldsymbol{\xi}_{0:T}$ to become conditionally Gaussian

$$\begin{aligned} h_t &= \mu + \kappa(h_{t-1} - \mu) + \eta_t \\ \eta_t | \xi_t &\stackrel{\text{iid}}{\sim} N(0, \xi_t^{-1}) \\ \xi_t &\stackrel{\text{iid}}{\sim} \text{PG}(1, 0), \end{aligned} \quad (3.4)$$

Algorithm 1: Gibbs sampling from joint posterior $p(\boldsymbol{\theta}_{0:T}, \mathbf{h}_{0:T}, \boldsymbol{\sigma}_{1:T}, \boldsymbol{\mu}, \boldsymbol{\kappa} | y_{1:T})$

Input: data $y_{1:T}$
initial $\boldsymbol{\mu}^{(0)}$, defaulting to $(\mu_0, \dots, \mu_0)^\top$, where μ_0 is the prior mean
initial $\boldsymbol{\kappa}^{(0)}$, defaulting to $(\kappa_0, \dots, \kappa_0)^\top$, where κ_0 is the prior mean
initial $\mathbf{h}_{1:T}^{(0)}$, defaulting to $h_{kt}^{(0)} = \mu_0$ for all k, t
initial $\boldsymbol{\sigma}_{1:T}^{(0)}$, defaulting to an estimate from the static seasonal AR
initial Pólya-Gamma variables $\boldsymbol{\xi}_{0:T}^{(0)}$, defaulting to 1 for all k, t
tuning parameters for PGAS
the number of posterior draws J

Run the particle filter to compute initial reference trajectory $\boldsymbol{\theta}_{0:T}^{(0)}$ for PGAS

for $j = 1$ **to** J **do**

$\backslash\backslash$ draw the parameter evolutions using PGAS or FFBSx

$\boldsymbol{\theta}_{0:T}^{(j)} \leftarrow \text{PGAS/FFBSx}(\boldsymbol{\theta}_{0:T} | \mathbf{h}_{0:T}^{(j-1)}, \boldsymbol{\sigma}_{1:T}^{(j-1)}, y_{1:T}, \boldsymbol{\theta}_{0:T}^{(j-1)})$

$\backslash\backslash$ draw the error standard deviations

$\boldsymbol{\sigma}_{1:T}^{(j)} \leftarrow p(\boldsymbol{\sigma}_{1:T} | \boldsymbol{\theta}_{0:T}^{(j)}, y_{1:T})$

for $k = 1$ **to** r **do in parallel**

$\backslash\backslash$ draw mixture of normals allocations

$\mathbf{a}_{k,1:T}^{(j)} \leftarrow p(\mathbf{a}_{k,1:T} | \boldsymbol{\theta}_{k,0:T}^{(j)}, h_{k,0:T}^{(j-1)})$

$\backslash\backslash$ draw log-volatilities

$\mathbf{h}_{k,0:T}^{(j)} \leftarrow p(\mathbf{h}_{k,0:T} | \boldsymbol{\theta}_{k,0:T}^{(j)}, \mathbf{a}_{k,1:T}^{(j)}, \kappa_k^{(j-1)}, \mu_k^{(j-1)}, \boldsymbol{\xi}_{k,1:T}^{(j-1)})$

$\backslash\backslash$ draw Pólya-Gamma variables

$\boldsymbol{\xi}_{k,0:T}^{(j)} \leftarrow p(\boldsymbol{\xi}_{k,0:T} | \mathbf{h}_{k,0:T}^{(j)}, \kappa_k^{(j-1)}, \mu_k^{(j-1)})$

$\backslash\backslash$ draw global mean log-volatility

$\mu_k^{(j)} \leftarrow p(\mu_k | \mathbf{h}_{k,1:T}^{(j)}, \kappa_k^{(j-1)}, \boldsymbol{\xi}_{k,1:T}^{(j)})$

$\backslash\backslash$ draw global log-volatility persistence

$\kappa_k^{(j)} \leftarrow p(\kappa_k | \mathbf{h}_{k,1:T}^{(j)}, \mu_k^{(j)}, \boldsymbol{\xi}_{k,1:T}^{(j)})$

end

end

Output: draws from the joint posterior of $\boldsymbol{\theta}_{0:T}, \mathbf{h}_{0:T}, \boldsymbol{\sigma}_{1:T}, \boldsymbol{\mu}$ and $\boldsymbol{\kappa}$.

where PG is the Pólya-Gamma distribution (Polson et al., 2013). Now, conditional on the mixture allocation $a_{1:T}$ and the Pólya-Gamma variables $\xi_{0:T}$, Kowal et al. (2019) combine the conditionally Gaussian likelihood from (3.2) with the conditionally Gaussian prior process in (3.4) to derive the posterior of $\mathbf{h}_{0:T}$ as multivariate normal. The inverse covariance matrix is tri-diagonal, which can be elegantly exploited for efficient sampling, see Rue (2001) and Kowal et al. (2019) for details.

To avoid numerical issues it is common to add an offset before taking logs in (3.2)

$$\log(\nu_t^2 + \text{offset}) = h_t + \log \epsilon_t^2, \quad (3.5)$$

for some small positive offset. With ν_t being the change in the parameter corresponding to h_t , this offset turns out to be important here since the dynamic shrinkage prior encourages parameters to stand still for extended periods, so ν_t tends to be close to zero for some t . The `dsp` package in R that accompanies Kowal et al. (2019) uses a different offset for each parameter and in each Gibbs sampling iteration following the rule

$$\text{offset} = \begin{cases} \max(10^{-8}, 10^{-6} \cdot \text{mad}(\nu_{1:T})) & \text{if } \nu_t^2 < 10^{-16} \text{ for any } t \\ 0 & \text{otherwise,} \end{cases} \quad (3.6)$$

where $\text{mad}(\mathbf{x})$ is the median absolute deviation for the elements in the vector \mathbf{x} . Section 4 further discusses the effect of the offset.

3.2 Updating the parameter paths

Conditional on all other parameters, the TVSAR model in (2.10) can be expressed as the following state-space model with $\boldsymbol{\theta}_t$ as the state vector

$$\boldsymbol{\theta}_0 \sim \text{Uniform}(\mathbb{S}) \quad (3.7)$$

$$\boldsymbol{\theta}_t | \boldsymbol{\theta}_{t-1} \sim N(\boldsymbol{\theta}_{t-1}, \text{Diag}(\exp(\mathbf{h}_t))) \quad (3.8)$$

$$y_t | \boldsymbol{\theta}_t \sim N(\mathbf{x}_t^\top \tilde{\mathbf{g}}(\boldsymbol{\theta}_t), \sigma^2), \quad (3.9)$$

where $\text{Uniform}(\mathbb{S})$ denotes the uniform distribution over the stability region for the implied ϕ_0 in each AR polynomial. Note that the state transitions in (3.8) is linear and heteroscedastic Gaussian, and the measurement model in (3.9) is nonlinear with Gaussian additive errors.

Our goal is to design a Gibbs updating step where we draw from the joint conditional posterior of the parameter paths $p(\boldsymbol{\theta}_{0:T} | y_{1:T}, \cdot)$, using the dot \cdot as a placeholder for all the other parameters in the model. Sampling is ideally performed by the following two steps:

1. compute the sequence of *filtering distributions* $p(\boldsymbol{\theta}_t | y_{1:t}, \cdot)$ for $t = 0, \dots, T$;
2. sample from the *joint smoothing distribution* $p(\boldsymbol{\theta}_{0:T} | y_{1:T}, \cdot)$ via backward sampling, starting from the final filtering distribution $p(\boldsymbol{\theta}_T | y_{1:T}, \cdot)$ and iterate back in time for $t = T, T - 1, \dots, 0$.

For linear Gaussian models, the filtering posteriors are Gaussian and can be computed recursively in closed form by the Kalman filter recursions. The backward sampling step then simulates from multivariate Gaussian distributions. This is the Forward Filtering and Backward Sampling (FFBS) algorithm developed by Carter and Kohn (1994) and Frühwirth-Schnatter (1994).

Conditional on the log-volatilities $\mathbf{h}_{0:T}$, the model in (3.7)-(3.9) is linear Gaussian in the transition model, but non-linear Gaussian in the measurement equation. There are a number of Sequential Monte Carlo (SMC) methods, also called particle methods, available for simulating from the joint smoothing posterior in non-Gaussian, non-linear state space models, see e.g. Chopin et al. (2020) and Lindsten and Schön (2013) for an overview.

Particle filters approximate the target filtering distribution, $p(\boldsymbol{\theta}_t|y_{1:t})$ by a set of N weighted particles, $\{\boldsymbol{\theta}_t^i, w_t^i\}_{i=1}^N$

$$\widehat{p}(\boldsymbol{\theta}_t|y_{1:t}) = \sum_{i=1}^N w_t^i \delta_{\boldsymbol{\theta}_t^i}(\boldsymbol{\theta}_t), \quad (3.10)$$

where $\sum_i w_t^i = 1$ and $\delta(\cdot)$ is the point mass Dirac delta function. The particles evolve in time based on a Markov proposal density $q_t(\boldsymbol{\theta}_t|\boldsymbol{\theta}_{t-1}, y_t)$ and are assigned importance weights w_t^i for the i th particle at time t . The particles at step t are resampled with replacement with probabilities proportional to w_t^i to form an unweighted sample from the filtering distribution $p(\boldsymbol{\theta}_t|y_{1:t})$. A particularly simple algorithm is the bootstrap particle filter which uses the model's transition density $f(\boldsymbol{\theta}_t|\boldsymbol{\theta}_{t-1})$ as proposal and the importance weights simplify to

$$w_t^i \propto g(y_t|\boldsymbol{\theta}_t^i)w_{t-1}^i, \quad (3.11)$$

where $g(y_t|\boldsymbol{\theta}_t)$ is the measurement density. The resampling step can be expressed as the sampling of ancestor indexes, a_t^i , where the outcome $a_t^i = j$ means that the i th particle at time t is propagated from the j th particle at time $t-1$ (Andrieu et al., 2010).

The Particle Gibbs (PG) sampler in Andrieu et al. (2010) samples from an SMC approximation conditioned on a prespecified reference trajectory. The Particle Gibbs with Ancestor Sampling (PGAS) algorithm in Lindsten et al. (2014) extends this algorithm by updating the ancestor of the reference trajectory at every time step t . Lindsten et al. (2014) show that the ancestral sampling step does not compromise the validity of the PG Markov kernel in Andrieu et al. (2010), and can greatly improve mixing. The PGAS algorithm approximates the joint smoothing density with a single forward sweep, unlike other methods that often require explicit forward and backward sweeps (Lindsten and Schön, 2013). Algorithm S1 in the Supplementary material summarizes the PGAS sampler with the bootstrap filter, and we refer to Lindsten et al. (2014) for further details. The PGAS algorithm can suffer from particle degeneracy in near-degenerate models (Lindsten et al., 2015), for example when the innovations in the transition model have close to zero variance for some t . This often occurs with the TVSAR in (2.10) since the dynamic shrinkage priors encourage parameters to remain constant for extended time periods.

For near-degenerate TVSAR models we suggest an alternative updating step for $\theta_{0:T}$ based on an approximate sampling step that replaces the Kalman filter in the FFBS sampler with the extended Kalman filter (EKF), see Thrun et al. (2005) for an introduction to the EKF. The algorithm uses the same backward simulation recursions as in the FFBS algorithm; we call this algorithm FFBSx, where x is a mnemonic for extended. The extended Kalman filter needs a Gaussian prior for the initial state. We therefore approximate the prior in Lemma 1 when using FFBSx by the closest normal distribution with respect to the Hellinger metric, see Section S1.2 for details.

The EKF linearizes the nonlinear observation and/or state equations via first-order Taylor expansions around the propagated state at each time step. The algorithm has been successfully applied to many nonlinear filtering problems (Cappé et al., 2007), but its accuracy depends on the degree of nonlinearity and how much the state and measurement noise deviate from Gaussian distributions. We show that it is very accurate for the TVSAR model, since the state transition remains linear and Gaussian and the non-linearity is only present in the observation equation, which still has additive Gaussian errors. Sections 4 and 5 show that the algorithm is fast, robust and accurate. The derivatives needed in the EKF are computed by automatic differentiation (Baydin et al., 2018), making it possible to write fast and general code for TVSAR with any number of seasonal periods.

4 Simulation experiments

4.1 Setup and benchmark models

We conduct three simulation experiments to assess the effectiveness of our methodology in handling scenarios involving changes in the regular and seasonal AR parameters – whether sudden, gradual, or constant over time. We simulate 100 time series from the data generating process for each experiment. The simulated time series consist of $T = 1000$ observations, and we perform 10 000 draws from the posterior distribution for each method, after a burn-in of 3000 iterations. The post burn-in draws are thinned by a factor of 10 before computing spectral densities, leaving 1000 thinned draws for the inference about the spectral density. In Experiments 1 and 2, we fit the same number of lags as the number of lags in the data generating process, while Experiment 3 assess the performance when the fitted models have more lags than the data generating process.

Our proposed models and algorithms are compared with the following alternatives: a linear time-varying AR model with dynamic shrinkage priors (Kowal et al., 2019) without explicit stationarity restrictions implemented in the R package `dsp`, a kernel smoothing estimation method using the `tvReg` package in R (Casas and Fernandez-Casal, 2023) and the time-varying AR with the static triple gamma shrinkage prior in the package `shrinkTVP` (Knaus et al., 2021)¹. We also compare with a spectral domain model, the `AdaptSpec` method for locally stationary time series (Rosen et al., 2012)

¹the dynamic triple gamma prior in Knaus and Frühwirth-Schnatter (2023) was added to the `shrinkTVP` package after these simulations were completed.

implemented in the R/C++ package `BayesSpec` (Bertolacci, 2021). `AdaptSpec` is a semi-parametric approach that divides the time series into segments in each MCMC iteration, and estimates a local spectral density using smoothing splines in each segment. We use default settings for all benchmark methods with the exception of `AdaptSpec` where the default number of spline knots is increased to 40 instead of the default with seven spline knots and the maximum number of segments is increased from the default 10 to 20. Preliminary experiments show that this gives `AdaptSpec` a better chance to capture the highly multimodal spectral density in seasonal models.

All of the time-varying AR benchmark models are designed for non-seasonal data. To give a fairer comparison, we construct seasonally adapted versions of the benchmark models. For example, a TVSAR with seasonality $\mathbf{s} = (1, 12)$ and lag orders $\mathbf{p} = (1, 1)$ can be formulated as a regular AR with $p + Ps = 13$ lags with lag polynomial

$$(1 - \phi_1 L)(1 - \Phi_2 L^{12}) = 1 - \phi_1 L - \Phi_2 L^{12} + \phi_1 \Phi_2 L^{13}. \quad (4.1)$$

If the data generating process is a TVSAR with seasonality $\mathbf{s} = (1, 12)$ and lag orders $\mathbf{p} = (1, 1)$, we fit benchmark models with 13 lags and impose zero-restrictions on the coefficients for lags 2 to 11. Note, however, that the coefficient on lag 13 is estimated as an unrestricted coefficient in the benchmark models since they cannot handle the non-linear multiplicative structure. The time-domain benchmark models do not impose stability/stationarity restrictions, and we therefore discard posterior draws outside the stability region to ensure a well-defined spectral density.

In all three experiments, we use iid priors for the static parameters: $\mu \sim N(-15, 3)$, $\kappa \sim \text{TN}(0.5, 0.3^2, -1, 1)$ and $\sigma^2 \sim \text{Inv-}\chi^2(3, s^2)$, where s^2 is the residual variance from a linear AR model fitted to the time series. Note that μ is on the log-scale, so the implied prior on the global standard deviation $\tau = \exp(\mu/2)$ is log normal with 95% equal tail interval $(2.92 \cdot 10^{-5}, 0.01)$. This prior encourages parameters to remain constant, but, as we will see, still allows for sizeable jumps via the heavy-tailed log-volatility innovations, η_t .

4.2 Performance metric

Since the benchmark methods include models in both the time and frequency domain, and the model comparison involves both models with a multiplicative structure and additive structure – where the parameters do not have the same interpretation – we compare the methods based on their ability to estimate the time-varying spectral density. The spectral density of a seasonal AR process at time t is given by (Wei, 2019)

$$f(t, \omega) = \frac{\sigma^2}{\pi} \frac{1}{|\phi_{pt}(e^{-i\omega})|^2} \frac{1}{|\Phi_{Pt}(e^{-is\omega})|^2} \text{ for } \omega \in (0, \pi) \text{ and } t = 1, \dots, T, \quad (4.2)$$

where ϕ_{pt} and Φ_{Pt} are the usual regular and seasonal AR lag polynomials at time t and $\omega \in (0, \pi]$ is the radial frequency. This expression extends to seasonal AR models with multiple seasonal periods in the obvious way. Following Rosen et al. (2012), we use the

Mean Square Errors (MSE) of the estimated log spectral density over all time periods as the performance metric

$$\text{MSE}(\widehat{\log f}) = \frac{1}{Tm} \sum_{t=1}^T \sum_{k=1}^m (\log \widehat{f}(t, \omega_k) - \log f(t, \omega_k))^2, \quad (4.3)$$

where $\log f(t, \omega)$ is the true log spectral density at time t and frequency ω , and $\widehat{\log f}(t, \omega)$ is its estimate, and $m = 314$ is the total number of frequencies on a grid from 0.01 to π . The posterior median of the log spectral density $\log f(t, \omega)$ is used as the point estimate in the Bayesian models since it is more robust to outliers in the MCMC.

4.3 Experiment 1 - Single-seasonal TVSAR

The first experiment simulates data from the time-varying TVSAR(\mathbf{s}, \mathbf{p}) with $\mathbf{s} = (1, 12)$ and $\mathbf{p} = (2, 2)$:

$$(1 - \phi_{1t}L - \phi_{2t}L^2)(1 - \Phi_{1t}L^{12} - \Phi_{2t}L^{24})y_t = \varepsilon_t, \quad (4.4)$$

where $\varepsilon_t \sim N(0, 1)$. The time evolution of the unrestricted non-seasonal parameters is

$$\theta_{1t} = \begin{cases} 0.8 \sin(\frac{\pi t}{T}) & \text{for } t = 1, \dots, 500 \\ -0.8 \sin(\frac{\pi t}{T}) & \text{for } t = 501, \dots, 1000 \end{cases} \quad (4.5)$$

$\theta_{2t} = -0.8$ for all t .

and the time evolution of the unrestricted seasonal parameters is

$$\Theta_{1t} = \begin{cases} -0.70 & \text{for } t = 1, \dots, 300 \\ 0 & \text{for } t = 301, \dots, 700 \\ 0.95 & \text{for } t = 701, \dots, 1000 \end{cases} \quad (4.6)$$

$\Theta_{2t} = -0.9$ for all t .

The beige lines in Figure 2 show the evolution of the regular AR parameters ϕ_{kt} and the seasonal AR parameters Φ_{kt} .

We first explore the numerical performance of the Gibbs sampler with a PGAS update step for different numbers of particles. As explained in Section 3.2, particle Gibbs samplers like PGAS can struggle when the state transition model is nearly degenerate. Our simulation setup is a rather extreme case of near-degeneracy where some parameters are constant over extended segments or even constant throughout time.

We compare PGAS with the more robust FFBSx algorithm based on the extended Kalman filter. The potential approximation errors from FFBSx can be attributed to the two non-linearities in the TVSAR: one from its the multiplicative structure and another from the stability restrictions. Therefore, we also apply the FFBSx algorithm to a TVSAR model without imposing the stationarity restrictions. The FFBSx applied

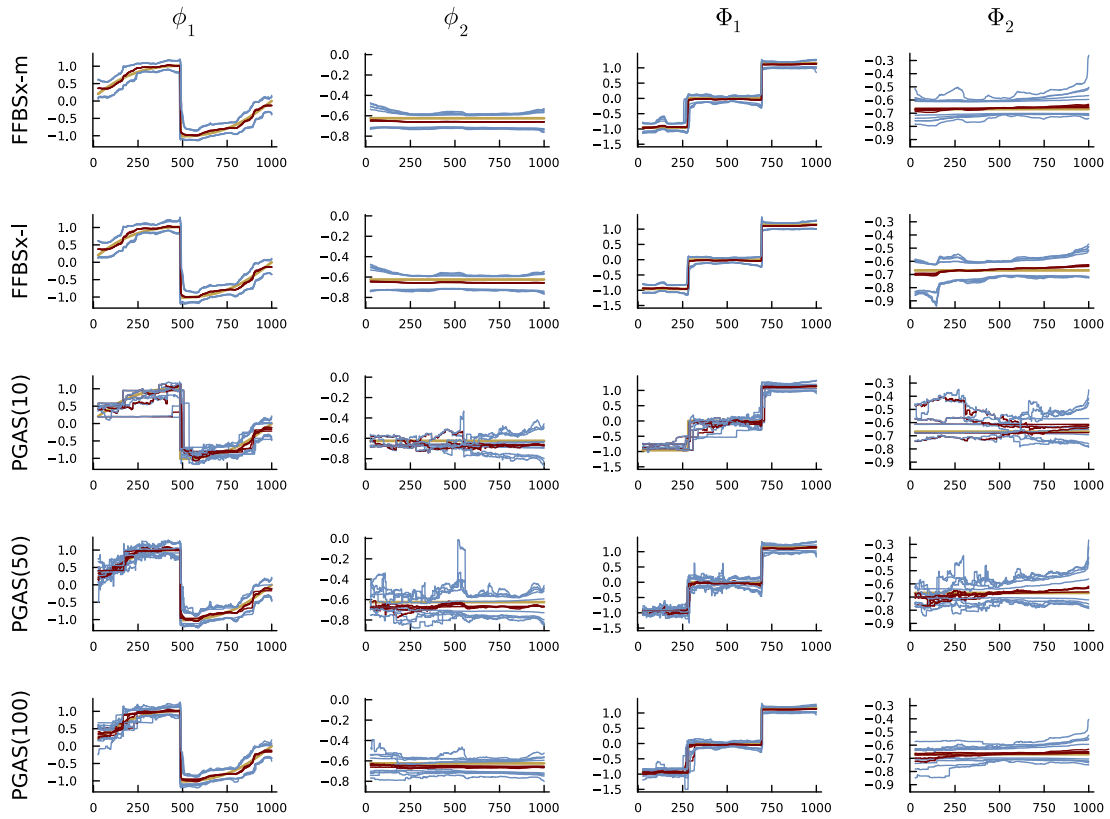


Figure 2: Experiment 1. Assessing MCMC convergence of different sampling algorithms by re-estimating the model using five different initial values drawn from the prior of the global hyperparameters μ and κ . All runs are for the same dataset. The red and blue lines are posterior medians and 95% equal tail credible bands over time for each of the five repeated runs. The beige line is the true parameter evolution given by (4.5) and (4.6) transformed to the stable parameterization.

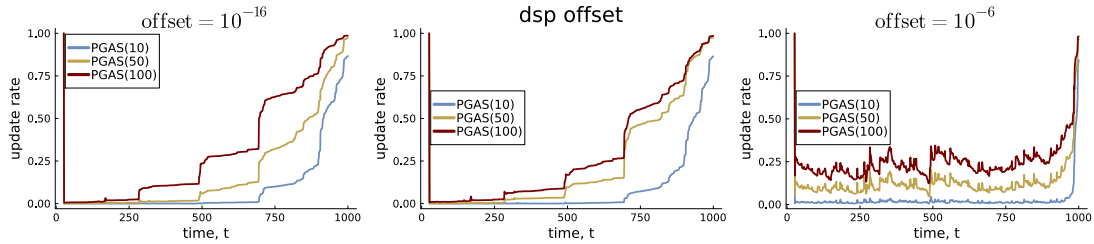


Figure 3: Experiment 1. PGAS update rates for three different offsets in the log-volatility model for \mathbf{h}_t for different number of particles.

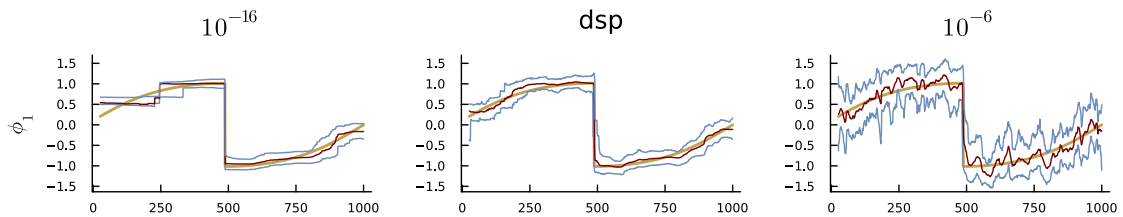


Figure 4: Experiment 1. Posterior median and 95% credible intervals for ϕ_{1t} from PGAS(100) from one run for the three different offsets in the log-volatility model for \mathbf{h}_t . See Figure S4 for the remaining parameters.

to the TVSAR with stationarity restrictions is referred to as FFBSx-m (where the m stands for the Monahan transformation in (2.3), while FFBSx-l refers to FFBSx applied to the TVSAR model without stationarity restrictions (l stands for linear).

Figure 2 assesses the convergence of the algorithms by plotting the posterior medians and equal-tail 95% credible intervals from five different runs on the same dataset, each with different initial values. The initial values for the global parameters are set so that $\mu_k = \mu$ and $\kappa_k = \kappa$ for all k , with μ and κ drawn from their respective priors in each run of the algorithm. The initial values for the log-volatilities $h_{k,t}$ are set to the randomly generated μ for all k and t . PGAS(N) is the PGAS algorithm with N particles. All PGAS algorithms use a proposal at time $t = 0$ from an initial FFBSx-m run with 500 iterations. The results in Figure 2 uses a minimal offset of 10^{-16} (close to the machine precision in Julia) in the update for $\mathbf{h}_{0:T}$; we return to this choice of offset below.

Figure 2 shows that both the FFBSx and PGAS samplers accurately capture the evolving patterns of varying complexities and correctly identify constant parameters. However, the PGAS sampler struggles with the near-degeneracy in this example, requiring at least 100 particles to achieve relatively stable results across different runs. In contrast, the FFBSx samplers are stabler, while yielding a very similar posterior to PGAS(100). This is reassuring since FFBSx is an approximate algorithm. Moreover, the additional nonlinearity handled by FFBSx-m compared to single nonlinearity in FFBSx-l does not deteriorate stability and fit.

The effective sample size (ESS) of the PGAS algorithms can be very low for the earlier part of the time period, while the ESS for the FFBSx algorithms are larger and stable

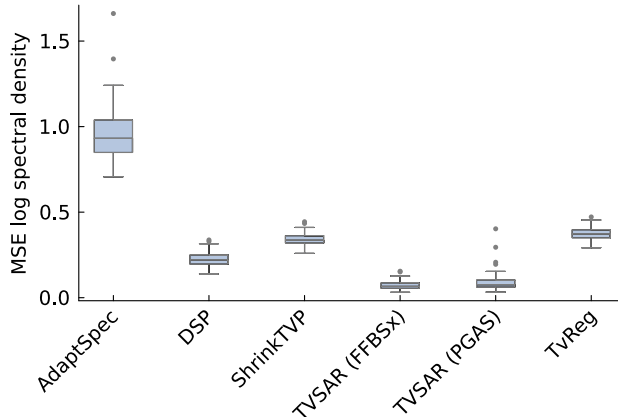


Figure 5: Experiment 1. Box plots of the MSE for the log spectral density over time and frequency from 100 simulated datasets.

across time; see Table S2 in Section S4.1 for ESS computed for the spectral density at some selected time periods and frequencies. The relatively low ESS comes from learning the global and local variances in the dynamic shrinkage process, a well known challenging issue with horseshoe-type of priors (Piironen and Vehtari, 2017), an area which would benefit from more research.

The FFBSx samplers are substantially faster than the PGAS samplers. One thousand draws with FFBSx-m takes 25 seconds, compared to 23 seconds for FFBSx-l and 258 seconds with PGAS(100). The timings are for Julia code on a single core of an Apple M1 processor with 16 GB of RAM memory. The robustness, speed and accuracy of FFBSx makes it our preferred algorithm. From now on, when we refer to the TVSAR model without mentioning the sampling algorithm, we mean the TVSAR with stationarity restrictions estimated with the FFBSx algorithm.

Figure 3 plots the update rates for the TVSAR parameters for the PGAS algorithms for three different offsets in the update for $\mathbf{h}_{1:T}$ in (3.6). The dsp offset uses the rule in (3.5) from the dsp package (Kowal et al., 2019). The update rate is the proportion of times the parameter changes over the iterations and is here computed on all 10 000 draws before thinning. A larger offset makes the state transition less degenerate with higher update rates, but with more wiggly parameter evolutions, making it harder to detect constant parameters; see Figure 4 for ϕ_{1t} and Figure S4 for the remaining parameters. Recall that the results in Figure 2 are based on the smallest offset 10^{-16} , showing that FFBSx works well even with essentially no offset. The effect of the near-degeneracy on PGAS can be less pronounced in other examples; see Experiment 2 below, and the results for TVSAR with one regular and one seasonal lag in Section S4.2.

Figure 5 displays box plots of the MSE metric in (4.3) for the compared models over the 100 simulated datasets. The TVSAR model estimated with the FFBSx algorithm performs best among the compared models, with a consistently low MSE across the datasets. The performance of the TVSAR model without stationarity restrictions is

similar and is not shown. The linear DSP model outperforms TvReg and the static triple Gamma prior in ShrinkTVP. AdaptSpec, which is not specifically designed for seasonal data, struggles here.

For completeness, we also compare the performance of the TVSAR model with a SARMA model with time invariant parameters in this experiment. Figure 5 does not show the MSE for this model, but it does, as expected, perform very poorly with a median MSE of 5.22. The static SARMA model is fitted with `auto.arima` in the `forecast` package in R, which automatically determines the optimal AR and MA lag orders; we allow for a maximal order of 5 for all regular and seasonal lags.

Figure 6 displays heatmaps of the estimated time-varying log spectral density for the different models. Following Rosen et al. (2012), we plot the posterior median of the time varying log spectral densities for three different datasets, corresponding to the 10%, 50%, and 90% percentiles of the MSE values for each method. This showcases how each method performs when it performs well (10%), average (50%), and poorly (90%). Note that the columns of Figure 6 are therefore for potentially different datasets for the different methods. Figure 7 gives an alternative view by plotting the estimated time-evolution at some selected frequencies. Our TVSAR model (with stationarity restrictions, estimated by FFBSx) gives less wiggly fits than DSP, while TvReg oversmooths, and ShrinkTVP both oversmooths the large jumps and has too much wiggle from period to period. Note that the recently added dynamic version of the triple Gamma prior in the ShrinkTVP may have better properties. Figure 8 plots the fitted log spectral densities at three different time points, again showing the fit for three different datasets selected from the MSE percentiles for each method.

4.4 Experiment 2 - Multi-seasonal TVSAR

This section shows the ability of our method to recover complex parameter patterns in the TVSAR models with two seasonal periods. The data generating process is the time-varying TVSAR(\mathbf{s}, \mathbf{p}) with $\mathbf{s} = (1, 4, 12)$ and $\mathbf{p} = (1, 1, 1)$:

$$(1 - \phi_{11t}L)(1 - \phi_{21t}L^4)(1 - \phi_{31t}L^{12})y_t = \varepsilon_t. \quad (4.7)$$

$$(4.8)$$

with $\varepsilon_t \sim N(0, 1)$. In the terminology of (2.5), the model comprises one regular non-seasonal component of order one and two seasonal components, each of order one, and with seasonal periods of four and twelve.

The time evolution of the unrestricted non-seasonal parameter is given by

$$\theta_{11t} = 0.8 \sin(\pi t/T) \text{ for } t = 1, \dots, 1000, \quad (4.9)$$

while the unrestricted parameter in the first seasonal period follows

$$\theta_{21t} = 0.5 \text{ for all } t \quad (4.10)$$

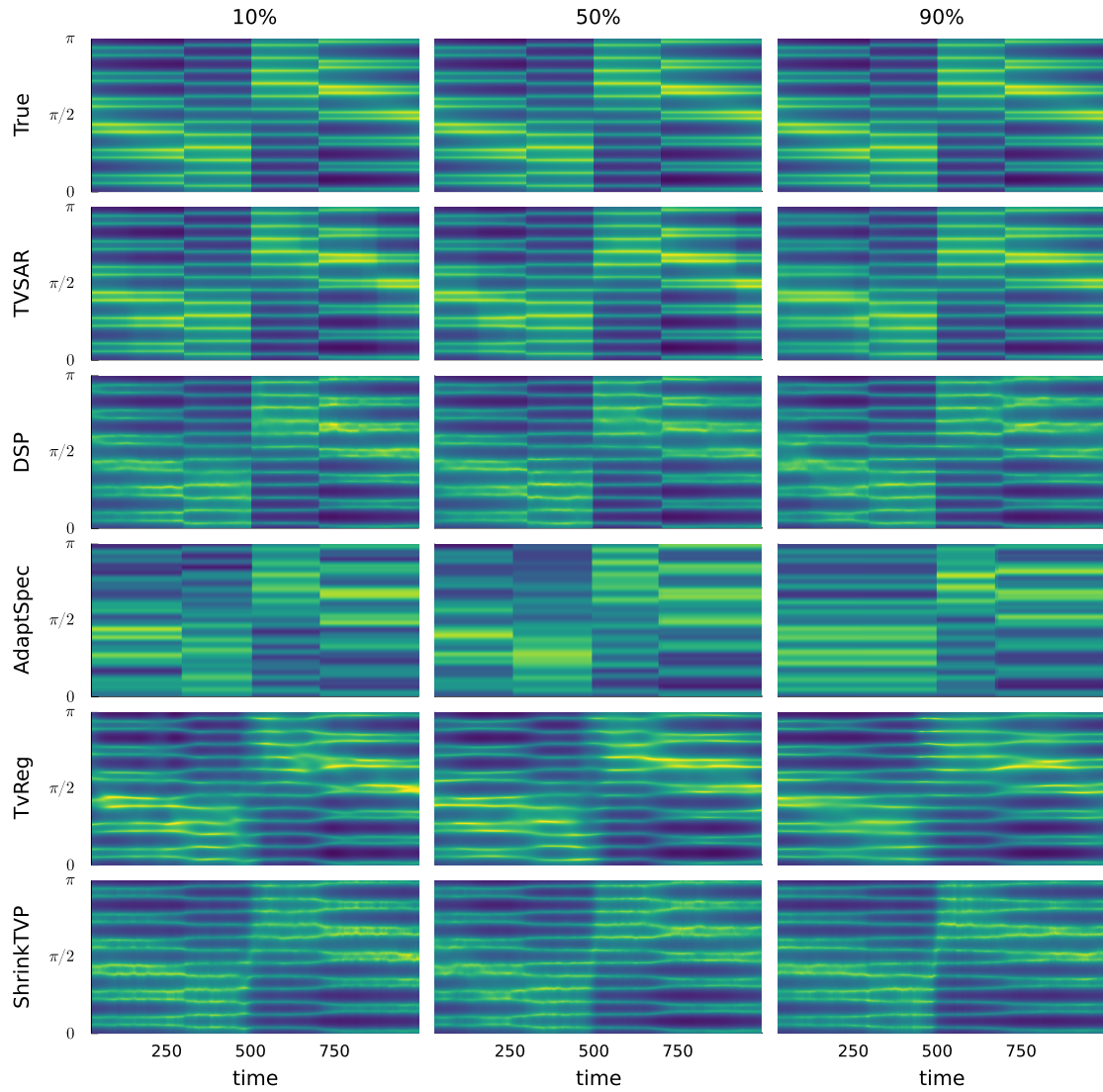


Figure 6: Experiment 1. Heatmaps of the estimated log spectral density over time for the different methods. The columns correspond to different datasets chosen from the percentiles of each model's MSE distribution, to showcase the performance of each model when it performs well (10%), average (50%) and poorly (90%).

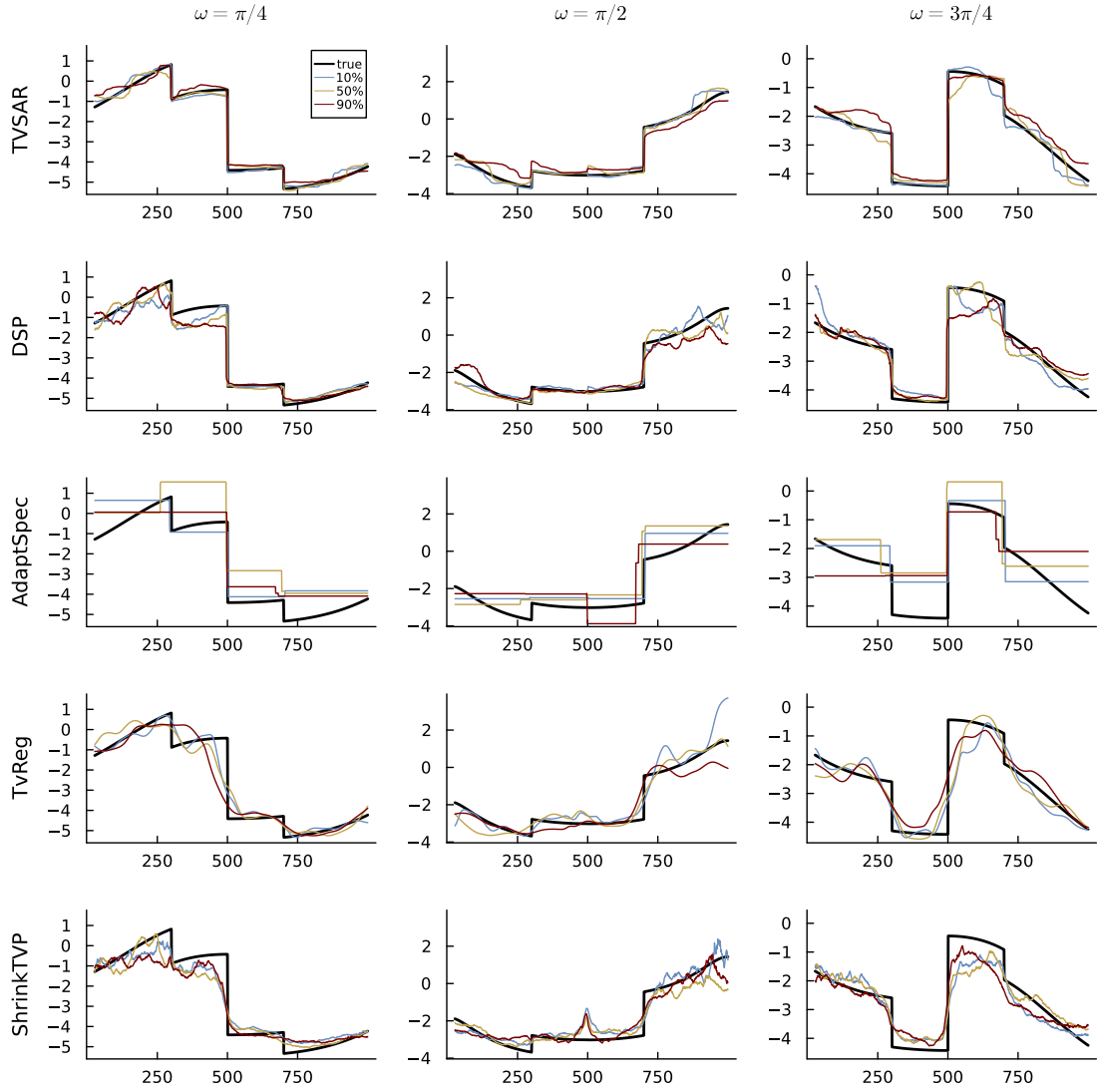


Figure 7: Experiment 1. Time evolution of the log spectral density at three different frequencies (columns) for several different model (rows). The black line is the true spectral density and the three colored lines are the posterior median estimates from three different datasets chosen from the MSE percentiles.

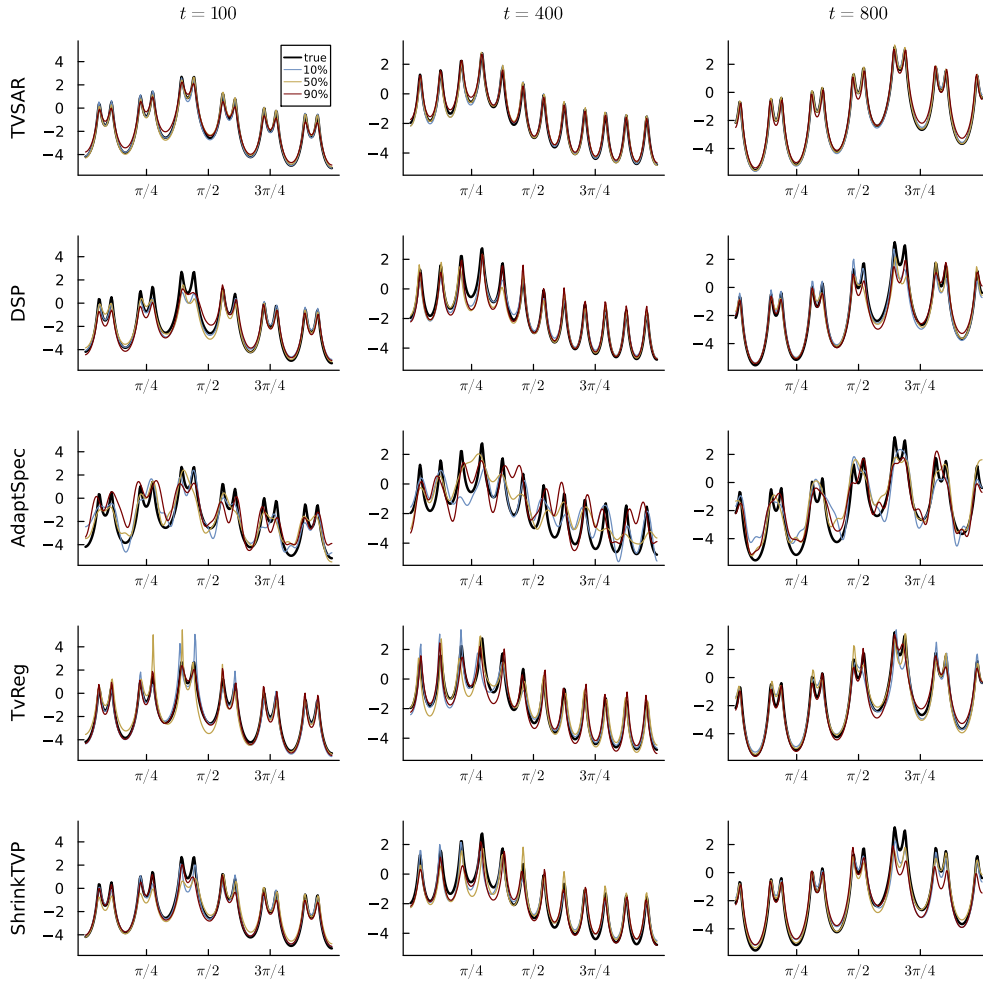


Figure 8: Experiment 1. Log spectral density at three different time points. The black line is the true spectral density and the three colored lines are the posterior medians from three different datasets chosen from the MSE percentiles.

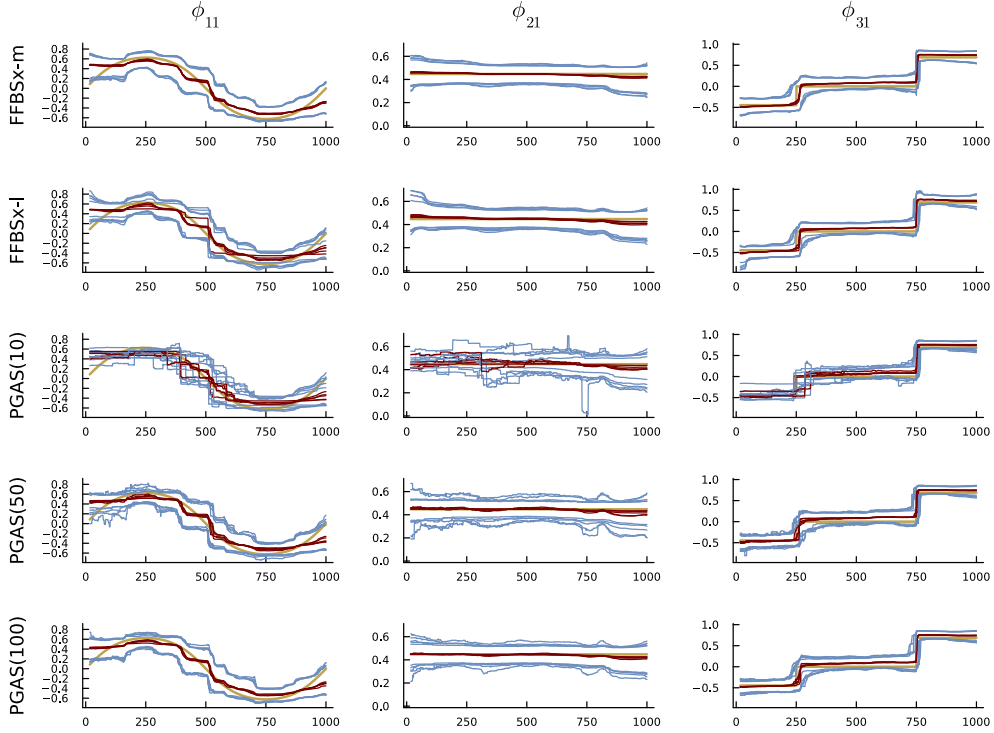


Figure 9: Experiment 2. Assessing MCMC convergence by re-estimating the model using five different initial values drawn from the prior of the global hyperparameters $\boldsymbol{\mu}$ and $\boldsymbol{\kappa}$. All runs are for the same dataset. The red and blue lines are posterior medians and 95% equal tail credible bands over time for each of the five repeated runs. The beige line is the true parameter evolution given by (4.9)-(4.11).

and for the second seasonal period

$$\theta_{31t} = \begin{cases} -0.50 & \text{for } t = 1, \dots, 250 \\ 0 & \text{for } t = 251, \dots, 750 \\ 0.95 & \text{for } t = 751, \dots, 1000. \end{cases} \quad (4.11)$$

Figure 9 shows that the posterior from the PGAS algorithm across different initial values is stabler compared to Experiment 1, but at least $N = 50$ particles are necessary. The PGAS update rates in Figure S11 are generally higher than in Experiment 1. The five runs of FFBSx-m are nearly identical and very close to the results from PGAS(100), showing that the extended Kalman filter is very accurate, even with both nonlinearities present in the model.

The left panel of Figure 10 displays box plots of the MSE for the log spectral density over 100 simulated datasets. The TVSAR model performs best, regardless of the sampling algorithm. TvReg performs best among the benchmark models. Figure S10

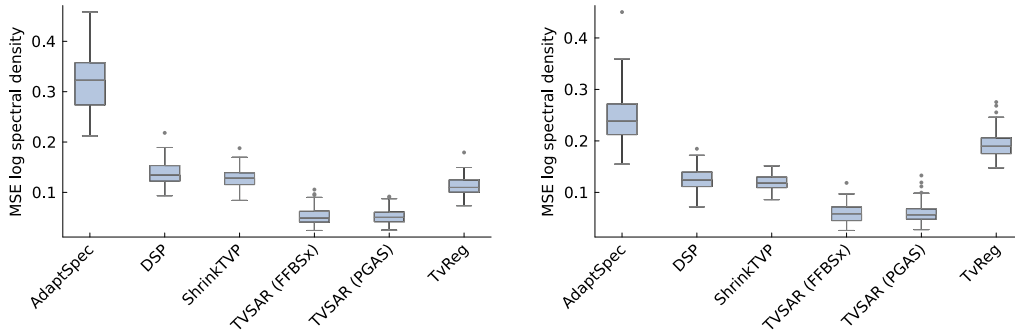


Figure 10: Experiment 2 (left) and Experiment 3 (right). Box plots of the MSE for the log spectral density over time and frequency from 100 simulated datasets.

in the supplementary material shows the estimated time-varying log spectral density for the different models, each with three different datasets chosen from the three percentiles of the MSE distribution for each method. Figures S12 and S13 show the estimated time evolution at some selected frequencies and the fitted log spectral densities at three different time points. The results are qualitatively similar to the corresponding results in Experiment 1.

4.5 Experiment 3 - Redundant lags

Experiments 1 and 2 use the correct number of regular and seasonal lags. In the empirical application in Section 5 we use log predictive scores to determine the optimal number of lags. This third and final experiment shows that the dynamic shrinkage prior is able to quite effectively shrink redundant lags to zero in the TVSAR when a model with too many lags is applied to the data. We simulate data from the model in Experiment 1, but with the coefficients for the second regular and second seasonal lags set to zero for all t . We then fit misspecified models with two regular and two seasonal lags.

The right panel of Figure 10 shows that the fitting a TVSAR($\mathbf{p} = (2, 2)$, $\mathbf{s} = (1, 12)$) to data from TVSAR($\mathbf{p} = (1, 1)$, $\mathbf{s} = (1, 12)$) still performs well, i.e. the TVSAR is able to shrink the time trajectory of redundant lags to zero for all t , see Figure 11. TvReg, which is the only time-domain model without shrinkage, clearly suffers from the redundant parameters and performs substantially worse than DSP and ShrinkTVP here. See Section S4.4 in the supplementary materials for detailed results.

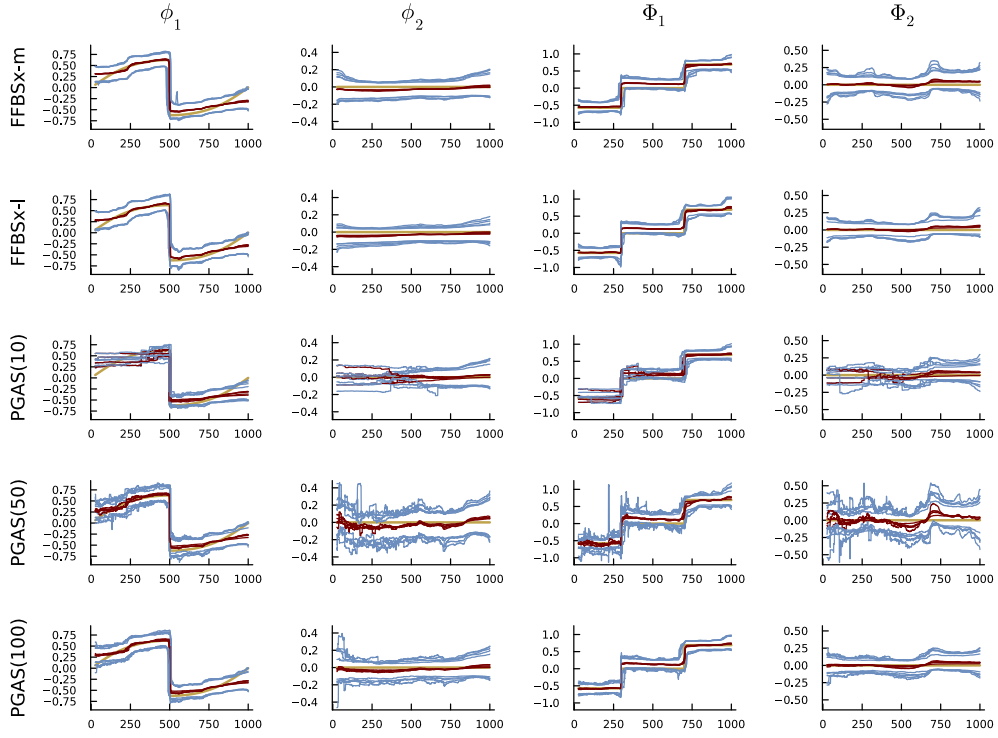


Figure 11: Experiment 3. Assessing MCMC convergence by re-estimating the model using five different initial values drawn from the prior of the global hyperparameters μ and κ . All runs are for the same dataset. The red and blue lines are posterior medians and 95% equal tail credible bands over time for each of the five repeated runs. The beige line is the true parameter evolution.

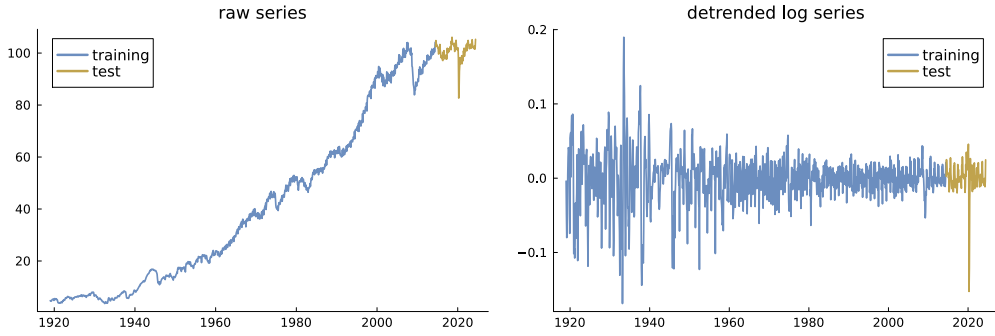


Figure 12: US industrial production time during Jan 1919 - June 2024. The test period used for model comparison, July 2014 - June 2024, is plotted in beige.

5 Application to US industrial production

We analyze monthly industrial production in the US between Jan 1919 - June 2024; the left panel in Figure 12 shows the data, with the test data used for model selection in beige. To focus on the time-varying AR parameters, we log and detrend the data prior to the analysis by subtracting a local mean estimated with the `TvReg` package. The right panel of Figure 12 shows the detrended data. Following Kowal et al. (2019), we do not remove the time-varying variance of the data. Instead, we add a stochastic volatility component for ε_t , where the log-volatility $g_t = \log \sigma_t^2$ is modeled as an AR(1) process. The parameter paths $g_{1:T}$, along with the mean log-volatility, the innovation variance, and persistence of the log-volatility process, are updated in separate Gibbs steps.

To determine a suitable number of regular lags p and seasonal lags P , Table 1 reports the out-of-sample log predictive score (LPS) for TVSAR models with different number of lags over the test period July 2014 - June 2024, with a total of 120 monthly observations. The most recent posterior distribution available at each time point is used when computing the predictive distribution. Note that this is a difficult period to forecast due to two massive outliers during the Covid-19 pandemic. The TVSAR(2,3) model has the highest LPS, but the more parsimonious TVSAR(1,2) is within one LPS unit of the TVSAR(2,3) model and will therefore be used here for illustration.

Figure 13 shows the posterior medians and 95% credible intervals for the AR coefficients in the TVSAR(1,2) model from 10 000 post burn-in draws obtained with the FFBSx algorithm. The regular AR coefficient in Figure 13 is stable over the century with only a mild downward trend. The two seasonal AR coefficients show substantial variation over time and jump to new levels during the Great Depression and WW2 period and the recent Covid-19 pandemic, while remaining very stable in the period in between these events. The posterior for the error standard deviation σ_t in the lower right graph of Figure 13 shows that there is a great deal of time-varying volatility in the data. Figure S17 shows that the FFBSx sampler has converged by plotting the posterior from three runs with different initial values drawn from the prior. PGAS with 100 particles gives a similar posterior to FFBSx, see Figure S18.

	P = 1	P = 2	P = 3
p = 1	363.08	<i>364.76</i>	364.81
p = 2	361.16	360.84	365.77
p = 3	357.13	365.47	365.65

Table 1: Log predictive scores (LPS) for 1-step-ahead forecasts over the 120 months test period July 2014 - June 2024 in the US industrial production data. The model with largest LPS is in bold font and the most parsimonious model within 1 LPS of the model with highest LPS is shown in italic.

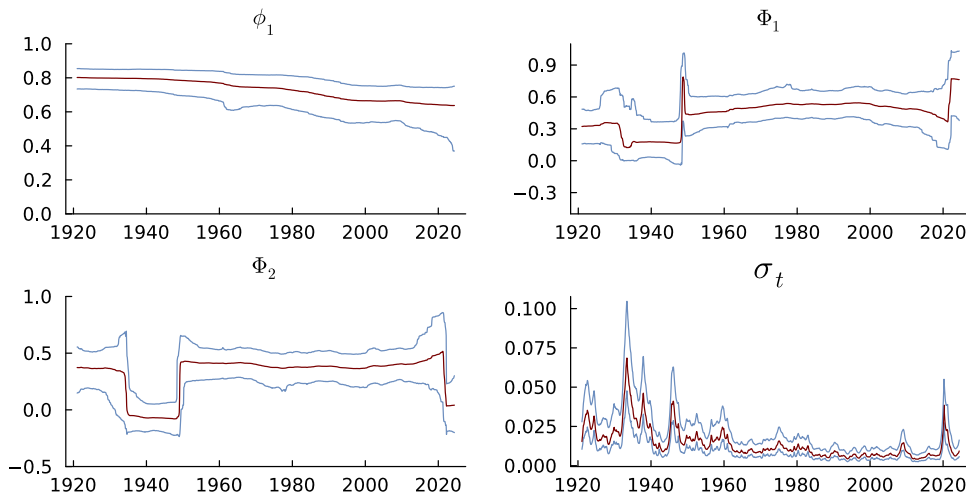


Figure 13: US industrial production. The posterior median and 95% credible intervals from the TVSAR(1,2) model with dynamic shrinkage prior and stochastic volatility, obtained with the FFBSx algorithm using an offset of 10^{-16} .

Figure 14 displays the posterior results from a TVSAR(1,2) model but with a traditional parameter evolution with homoscedastic Gaussian innovations. The results are qualitatively similar to the results from the dynamic shrinkage prior in Figure 13, but the parameter paths are much more wiggly in stable periods and oversmooth whenever there are jumps, a consequence of the constant parameter innovation variance.

Figures 15 and 16 illustrate the time-varying nature of the data and fitted model by plotting the time evolution of the log spectral density over time. The spectral density during the Great Depression and WW2 period has substantially less seasonal variation compared to other time periods, and the Covid-19 pandemic also stands out. Fitting a SAR(1,2) with constant parameters gives posterior median estimates $\hat{\phi}_1 = 0.759$, $\hat{\Phi}_1 = 0.539$ and $\hat{\Phi}_2 = 0.356$ and a fitted spectral density (beige line in Figure 16) dominated by the long stable period 1950-2020.

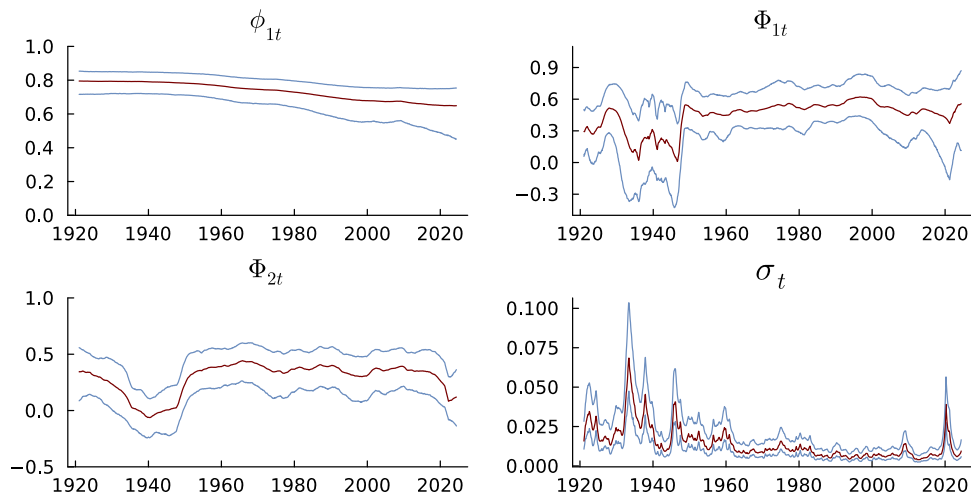


Figure 14: US industrial production. Posterior from TVSAR(1,2) model with homoscedastic Gaussian parameter innovations and stochastic volatility, obtained with the FFBSx algorithm.

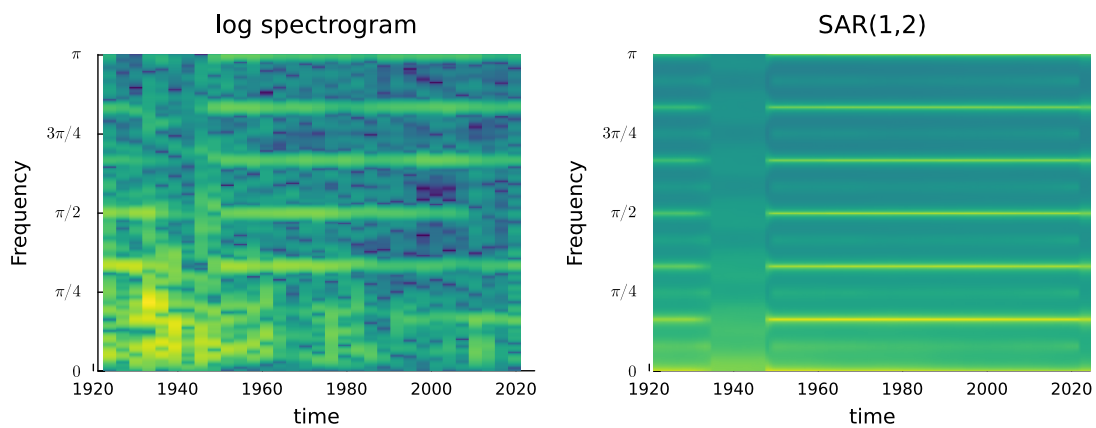


Figure 15: US industrial production. Left: Nonparametric log spectral density over time estimated by Hanning tapered periodograms over overlapping sliding windows of 120 months, moving 36 months between each window; note that 18 months (half the window width) are lost in the beginning and at the end of the time period. Right: posterior median time varying log spectral density from the TVSAR(1,2) model.

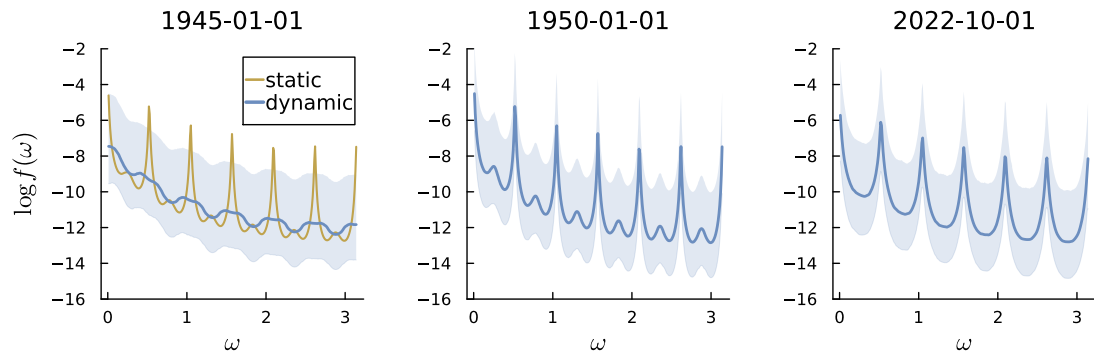


Figure 16: US industrial production. Fitted spectral density at three different time periods from TVSAR(1,2) model with time-varying parameters (blue line is posterior median and light blue bands are 95% credible intervals) and static parameters (beige line is posterior median). Both models have time-varying error variance. An interactive graph in javascript is available at <https://observablehq.com/@mattiasvillani/tvsar-spectral-usip>

6 Conclusions

Our article proposes a time-varying multi-seasonal AR model with the parameters in the non-seasonal and the seasonal polynomials following the dynamic shrinkage process priors in Kowal et al. (2019). We show empirically that the model can capture extended periods of constant parameters, periods of rapid changes and abrupt jumps, as well as shrinking away redundant lags. In every time period the freely evolving parameters are mapped to the region of stable AR parameters to ensure that parameters do not drift into explosive regions. Our framework can be used with any of the recently developed global-local shrinkage priors, for example the prior processes in Kalli and Griffin (2014), Cadonna et al. (2020) and Knaus and Frühwirth-Schnatter (2023). The model allows for multiple seasonal periods, which is a common feature in modern datasets where data is often observed hourly or at even high frequencies. The seasonalities are modelled with the parsimonious multiplicative structure in Box et al. (2015).

Our algorithm samples from the joint posterior distribution of all the model parameters by Gibbs sampling. The multiplicative model structure and the restriction to a stable process makes the model nonlinear and the update step for the time-varying AR parameters challenging. We propose the FFBSx sampler based on the extended Kalman filter. We show that this approximate sampler is accurate by comparing its posterior with PGAS (Lindsten et al., 2014), a state-of-the-art particle MCMC sampler which is known to be simulation consistent. The FFBSx sampler is fast, accurate and robust to the near-degeneracy in the state transition caused by the dynamic shrinkage process prior. The gradient in the FFBSx algorithm is efficiently computed by automatic differentiation, making it easy to write general computer code for any number of seasonal AR polynomials.

The model and inference method are explored in three simulated examples with different numbers of seasonalities, and shown to compare well to several benchmarks.

An application to more than a century of monthly US industrial production data detects interesting and large changes in seasonality during the Great Depression and the recent Covid-19 pandemic, separated by a long period of remarkably constant seasonality.

An extension of the model to the ARMA case with the exact likelihood function is in progress. The extension to a seasonal vector AR and ARMA model is possible using the multivariate stability and invertibility restrictions in Ansley and Kohn (1986), but care is needed to handle the much larger number of parameters. We also plan to explore the forecasting performance of the proposed model in a separate article. Future research should also explore the potential interplay between time-varying AR parameters and a time-varying mean of the process.

Acknowledgments

Mattias Villani was partially funded by the Swedish Research Council, grant 2020-02846.

References

- Andrieu, C., Doucet, A., and Holenstein, R. (2010). Particle Markov chain Monte Carlo methods. *Journal of the Royal Statistical Society Series B*, 72(3):269–342.
- Ansley, C. F. and Kohn, R. (1986). A note on reparameterizing a vector autoregressive moving average model to enforce stationarity. *Journal of Statistical Computation and Simulation*, 24(2):99–106.
- Barndorff-Nielsen, O., Kent, J., and Sørensen, M. (1982). Normal variance-mean mixtures and z distributions. *International Statistical Review*, pages 145–159.
- Barndorff-Nielsen, O. and Schou, G. (1973). On the parametrization of autoregressive models by partial autocorrelations. *Journal of Multivariate Analysis*, 3(4).
- Baydin, A. G., Pearlmutter, B. A., Radul, A. A., and Siskind, J. M. (2018). Automatic differentiation in machine learning: a survey. *Journal of machine learning research*, 18(153):1–43.
- Bertolacci, M. (2021). BayesSpec. <https://github.com/mbertolacci/BayesSpec.git>.
- Box, G. and Jenkins, G. M. (1970). *Time Series Analysis: Forecasting and Control*. San Francisco: Holden-Day, first edition.
- Box, G. E., Jenkins, G. M., Reinsel, G. C., and Ljung, G. M. (2015). *Time series analysis: forecasting and control*. John Wiley & Sons, fifth edition.
- Cadonna, A., Frühwirth-Schnatter, S., and Knaus, P. (2020). Triple the gamma—a unifying shrinkage prior for variance and variable selection in sparse state space and tvp models. *Econometrics*, 8(2):20.

- Cappé, O., Godsill, S. J., and Moulines, E. (2007). An overview of existing methods and recent advances in sequential Monte Carlo. *Proceedings of the IEEE*, 95(5):899–924.
- Carter, C. K. and Kohn, R. (1994). On Gibbs sampling for state space models. *Biometrika*, 81(3):541–553.
- Carvalho, C. M., Polson, N. G., and Scott, J. G. (2010). The horseshoe estimator for sparse signals. *Biometrika*, 97(2):465–480.
- Casas, I. and Fernandez-Casal, R. (2023). *tvReg: Time-Varying Coefficients Linear Regression for Single and Multi-Equations*. R package version 0.5.9.
- Chib, S. (1998). Estimation and comparison of multiple change-point models. *Journal of econometrics*, 86(2):221–241.
- Chopin, N., Papaspiliopoulos, O., et al. (2020). *An introduction to sequential Monte Carlo*, volume 4. Springer.
- Dahlhaus, R. (2000). A likelihood approximation for locally stationary processes. *The Annals of Statistics*, 28(6):1762–1794.
- De Livera, A. M., Hyndman, R. J., and Snyder, R. D. (2011). Forecasting time series with complex seasonal patterns using exponential smoothing. *Journal of the American Statistical Association*, 106(496):1513–1527.
- Doan, T., Litterman, R., and Sims, C. (1984). Forecasting and conditional projection using realistic prior distributions. *Econometric reviews*, 3(1):1–100.
- Everitt, R. G., Andrieu, C., and Davy, M. (2013). Online Bayesian inference in some time-frequency representations of non-stationary processes. *IEEE transactions on signal processing*, 61(22):5755–5766.
- Frühwirth-Schnatter, S. (1994). Data augmentation and dynamic linear models. *Journal of time series analysis*, 15(2):183–202.
- Gerlach, R., Carter, C., and Kohn, R. (2000). Efficient Bayesian inference for dynamic mixture models. *Journal of the American Statistical Association*, 95(451):819–828.
- Godsill, S. J., Doucet, A., and West, M. (2004). Monte Carlo smoothing for nonlinear time series. *Journal of the American Statistical Association*, 99(465):156–168.
- Granger, C. W. and Joyeux, R. (1980). An introduction to long-memory time series models and fractional differencing. *Journal of time series analysis*, 1(1):15–29.
- Hamilton, J. D. (1989). A new approach to the economic analysis of nonstationary time series and the business cycle. *Econometrica*, pages 357–384.
- Hamilton, J. D. (2020). *Time series analysis*. Princeton university press.

- Jones, M. C. (1987). Randomly choosing parameters from the stationarity and invertibility region of autoregressive-moving average models. *Journal of the Royal Statistical Society. Series C (Applied Statistics)*, 36(2):134–138.
- Jones, M. C. and Faddy, M. (2003). A skew extension of the t-distribution, with applications. *Journal of the Royal Statistical Society Series B: Statistical Methodology*, 65(1):159–174.
- Kalli, M. and Griffin, J. E. (2014). Time-varying sparsity in dynamic regression models. *Journal of Econometrics*, 178(2):779–793.
- Kastner, G. and Frühwirth-Schnatter, S. (2014). Ancillarity-sufficiency interweaving strategy (ASIS) for boosting MCMC estimation of stochastic volatility models. *Computational Statistics & Data Analysis*, 76:408–423.
- Kim, S., Shephard, N., and Chib, S. (1998). Stochastic volatility: likelihood inference and comparison with arch models. *The review of economic studies*, 65(3):361–393.
- Knaus, P., Bitto-Nemling, A., Cadonna, A., and Frühwirth-Schnatter, S. (2021). Shrinkage in the time-varying parameter model framework using the R package shrinkTVP. *Journal of Statistical Software*, 100(13).
- Knaus, P. and Frühwirth-Schnatter, S. (2023). The dynamic triple gamma prior as a shrinkage process prior for time-varying parameter models. *arXiv preprint arXiv:2312.10487*.
- Kowal, D. R., Matteson, D. S., and Ruppert, D. (2019). Dynamic shrinkage processes. *Journal of the Royal Statistical Society: Series B (Statistical Methodology)*, 81(4):781–804.
- Lindsten, F., Bunch, P., Singh, S. S., and Schön, T. B. (2015). Particle ancestor sampling for near-degenerate or intractable state transition models. *arXiv preprint arXiv:1505.06356*.
- Lindsten, F., Jordan, M. I., and Schon, T. B. (2014). Particle Gibbs with ancestor sampling. *Journal of Machine Learning Research*, 15:2145–2184.
- Lindsten, F. and Schön, T. B. (2013). Backward simulation methods for Monte Carlo statistical inference. *Foundations and Trends in Machine Learning*, 6(1):1–143.
- Lubik, T. A. and Matthes, C. (2015). Time-varying parameter vector autoregressions: Specification, estimation, and an application. *Economic Quarterly*, 101(46):323–352.
- Makridakis, S. and Hibon, M. (1997). ARMA models and the Box–Jenkins methodology. *Journal of forecasting*, 16(3):147–163.
- Monahan, J. F. (1984). A note on enforcing stationarity in autoregressive-moving average models. *Biometrika*, 71(2):403–404.

- Omori, Y., Chib, S., Shephard, N., and Nakajima, J. (2007). Stochastic volatility with leverage: Fast and efficient likelihood inference. *Journal of Econometrics*, 140(2):425–449.
- Piironen, J. and Vehtari, A. (2017). Sparsity information and regularization in the horseshoe and other shrinkage priors. *Electronic Journal of Statistics*, 11:5018–5051.
- Polson, N. G., Scott, J. G., and Windle, J. (2013). Bayesian inference for logistic models using Pólya–gamma latent variables. *Journal of the American Statistical Association*, 108(504):1339–1349.
- Prado, R. and West, M. (2010). *Time series: modeling, computation, and inference*. Chapman and Hall/CRC.
- Primiceri, G. E. (2005). Time varying structural vector autoregressions and monetary policy. *The Review of Economic Studies*, 72(3):821–852.
- Rosen, O., Wood, S., and Stoffer, D. S. (2012). Adaptspec: Adaptive spectral estimation for nonstationary time series. *Journal of the American Statistical Association*, 107(500):1575–1589.
- Rue, H. (2001). Fast sampling of Gaussian Markov random fields. *Journal of the Royal Statistical Society: Series B (Statistical Methodology)*, 63(2):325–338.
- Smith, J. and Yadav, S. (1994). Forecasting costs incurred from unit differencing fractionally integrated processes. *International Journal of Forecasting*, 10(4):507–514.
- Thrun, S., Burgard, W., and Fox, D. (2005). *Probabilistic robotics*. MA: MIT Press.
- Wei, W. (2019). *Time Series Analysis Univariate and Multivariate Methods*. Pearson Modern Classics for Advanced Statistics Series. Pearson Education.
- Wood, S., Rosen, O., and Kohn, R. (2011). Bayesian mixtures of autoregressive models. *Journal of Computational and Graphical Statistics*, 20(1):174–195.
- Xie, T. and Ding, J. (2020). Forecasting with multiple seasonality. In *2020 IEEE International Conference on Big Data (Big Data)*, pages 240–245. IEEE.
- Yang, W.-H., Holan, S., and Wikle, C. (2014). Bayesian lattice filters for time-varying autoregression and time-frequency analysis. *Bayesian Analysis*, 11.

Supplement to Time-Varying Multi-Seasonal AR Models

Ganna Fagerberg^{a*}, Mattias Villani^a and Robert Kohn^{b,c}

This Supplement contains proofs and additional results for the paper *Time-Varying Multi-Seasonal AR Models*.

S1 Uniform distribution on the stability region

S1.1 Proof of Lemma 1

A random variable $X \sim t_{\text{skew}}(a, b)$, where $a >$ and $b > 0$ are parameters, follows the skew- t distribution in Jones and Faddy (2003) if it has density

$$f(x) = \frac{1}{2^{a+b-1} \text{B}(a, b) \sqrt{a+b}} \left(1 + \frac{x}{\sqrt{a+b+x^2}}\right)^{a+1/2} \left(1 - \frac{x}{\sqrt{a+b+x^2}}\right)^{b+1/2} \quad (\text{S1.1})$$

One characterization of this distribution is that if $Y \sim \text{Beta}(a, b)$ then

$$X = \sqrt{a+b} \frac{2Y-1}{2\sqrt{Y(1-Y)}} \sim t_{\text{skew}}(a, b).$$

More generally, $X \sim t_{\text{skew}}(a, b, \mu, \sigma)$ follows from a location-scale transformation $X \rightarrow \mu + \sigma X$.

Jones (1987) proves that if the partial autocorrelations are independently distributed as

$$r_k \sim \text{Beta}_{(-1,1)}(\alpha = \lfloor (k+1)/2 \rfloor, \beta = \lfloor k/2 \rfloor + 1), \quad (\text{S1.2})$$

where $\lfloor x \rfloor$ is the integer part of x , $k = 1, \dots, p$, and $\text{Beta}_{(-1,1)}$ denotes the Beta distribution shifted to the interval $(-1, 1)$, then the implied distribution for the AR coefficients is uniform over the stability/stationary region in ϕ -space.

*Corresponding author: ganna.fagerberg@stat.su.se. ^aDepartment of Statistics, Stockholm University.

^bSchool of Business, University of New South Wales. ^cData Analytics Center for Resources and Environments (DARE).

	θ_1	θ_2	θ_3	θ_4	θ_5	θ_6	θ_7	θ_8	θ_9	θ_{10}
mean	0	-0.53	0	-0.264	0	-0.175	0	-0.13	0	-0.103
stdev	1.042	0.858	0.622	0.558	0.475	0.441	0.397	0.375	0.348	0.332

Table S1: Normal approximation of the student-t and skew-t distributions in Lemma 1 that minimizes the Hellinger distance.

Let $q_k \sim \text{Beta}(\alpha_k = \lfloor (k+1)/2 \rfloor, \beta_k = \lfloor k/2 \rfloor + 1)$ follow the usual Beta distribution over $(0, 1)$ so that, by definition, $r_k \stackrel{d}{=} 2q_k - 1$, where $\stackrel{d}{=}$ denotes equality in distribution. Since $r_k = \theta_k / \sqrt{1 + \theta_k^2}$, we have

$$\theta_k = \frac{r_k}{\sqrt{1 - r_k^2}} \stackrel{d}{=} \frac{2q_k - 1}{\sqrt{1 - (2q_k - 1)^2}} = \frac{2q_k - 1}{2\sqrt{q_k(1 - q_k)}} = \frac{1}{\sqrt{k+1}} T$$

where

$$T = \sqrt{k+1} \frac{2q_k - 1}{2\sqrt{q_k(1 - q_k)}}$$

Since $\alpha_k + \beta_k = k + 1$ for all k , we have $T \sim t_{\text{skew}}(\alpha_k, \beta_k)$ (Jones and Faddy, 2003). This shows that $\theta_k \sim t_{\text{skew}}(\alpha_k, \beta_k, 0, 1/\sqrt{k+1})$ for all k . When k is even, we have $\alpha_k = k/2$ and $\beta_k = (k+2)/2$. When k is odd, we have $\alpha_k = \beta_k$ and the skew-t distribution reduces to the symmetric student-t distribution with $2\alpha_k = k + 1$ degrees of freedom (Jones and Faddy, 2003), and hence $\theta_k \sim t(k+1, 0, 1/\sqrt{k+1})$, which proves the result in Lemma 1.

S1.2 Normal approximation

The FFBSx algorithm requires a multivariate normal distribution for the initial state θ_0 . We therefore approximate the student- t and skew- t distributions in Lemma 1 by independent univariate normal distributions by finding the closest normal approximation as measured by the Hellinger distance

$$H^2(p, q) = \frac{1}{2} \int_{\mathcal{X}} \left(\sqrt{p(x)} - \sqrt{q(x)} \right)^2 dx. \quad (\text{S1.3})$$

For the symmetric student- t case, we minimize with respect to the standard deviation, while for the skew- t , we minimize with respect to both the mean and standard deviation of the approximating normal. The optimal normal approximation is listed in Table S1 for up to 10 AR lags. Figure S1 shows that the implied distribution on the stability region from the normal approximation (middle) is close to the ideal uniform distribution (left). The panel to the right shows the implied distribution on ϕ_1 and ϕ_2 from a $N(0, 3^2)$ distribution for each θ_k as a reference, showing that this prior puts most of its prior mass close to the boundaries of the stability region.

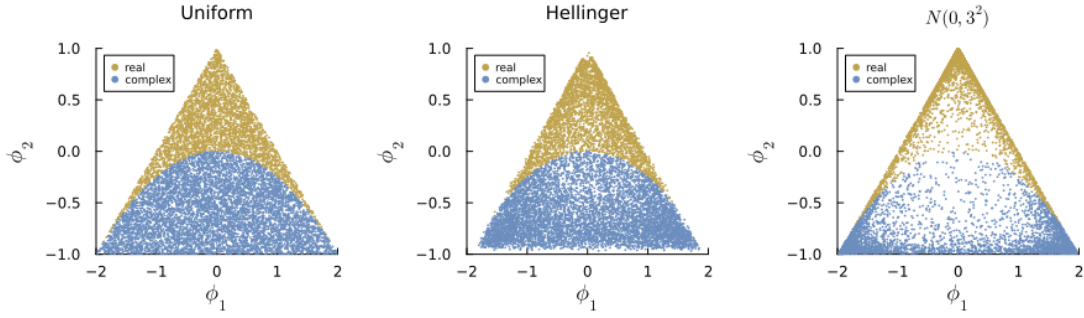


Figure S1: Illustrating 10000 draws from the uniform distribution in Lemma 1 (left) and the optimal normal approximation in Table S1 (middle). The implied distribution from a $N(0, 3^2)$ prior for both θ_1 and θ_2 is shown as reference (right). The beige points are draws with real roots in the AR polynomial while the blue points are draws with complex roots.

S2 Particle Gibbs with Ancestor Sampling

A general SSM with state vector $\boldsymbol{\theta}_t$ and measurements y_t is of the form

$$\begin{aligned}\boldsymbol{\theta}_0 &\sim f_0(\boldsymbol{\theta}_0) \\ \boldsymbol{\theta}_t &\sim f(\boldsymbol{\theta}_t|\boldsymbol{\theta}_{t-1}) \\ y_t &\sim g(y_t|\boldsymbol{\theta}_t),\end{aligned}\tag{S2.1}$$

where f_0 is the initial prior, $f(\boldsymbol{\theta}_t|\boldsymbol{\theta}_{t-1})$ is the state transition model and $g(y_t|\boldsymbol{\theta}_t)$ is the measurement model.

Particle filters approximate the target filtering distribution, $p(\boldsymbol{\theta}_t|y_{1:t})$ by a set of N weighted particles, $\{\boldsymbol{\theta}_t^i, w_t^i\}_{i=1}^N$

$$\hat{p}(\boldsymbol{\theta}_t|y_{1:t}) = \sum_{i=1}^N w_t^i \delta_{\boldsymbol{\theta}_t^i}(\boldsymbol{\theta}_t),\tag{S2.2}$$

where $\sum_i w_t^i = 1$ and $\delta(\cdot)$ is the point mass Dirac delta function. The particles evolve in time based on a Markov proposal density $q_t(\boldsymbol{\theta}_t|\boldsymbol{\theta}_{t-1}, y_t)$ and are assigned importance weights

$$w_t^i \propto \frac{g(y_t|\boldsymbol{\theta}_t^i) f(\boldsymbol{\theta}_t^i|\boldsymbol{\theta}_{t-1}^i)}{q_t(\boldsymbol{\theta}_t^i|\boldsymbol{\theta}_{t-1}^i, y_t)} w_{t-1}^i,\tag{S2.3}$$

where $g(y_t|\boldsymbol{\theta}_t)$ is the measurement density and $f(\boldsymbol{\theta}_t|\boldsymbol{\theta}_{t-1})$ is the transition density. The particles at step t are resampled with replacement with probabilities proportional to w_t^i to form an unweighted sample from the filtering distribution $p(\boldsymbol{\theta}_t|y_{1:t})$. A particularly simple algorithm is the bootstrap particle filter which uses the model's transition density $f(\boldsymbol{\theta}_t|\boldsymbol{\theta}_{t-1})$ as proposal and the importance weights in (S2.3) simplify to

$$w_t^i \propto g(y_t|\boldsymbol{\theta}_t^i) w_{t-1}^i.\tag{S2.4}$$

The resampling step can be expressed as the sampling of ancestor indexes, a_t^i , where the outcome $a_t^i = j$ means that the i th particle at time t is propagated from the j th particle at time $t - 1$ (Andrieu et al., 2010).

Particle filters often face degeneracy problems with only a few particles carrying significant weight. The resampling step partially addresses this problem, but frequent resampling can lead to a loss of particle diversity. To address this, it is common to resample only when the estimated effective sample size

$$\text{ESS}_{t-1} := \frac{1}{\sum_{i=1}^N (w_{t-1}^i)^2} \quad (\text{S2.5})$$

is below a certain threshold ESS_{\min} . We use $\text{ESS}_{\min} = N/2$ and systematic resampling (Chopin et al., 2020, Ch. 9) as default settings.

Andrieu et al. (2010) introduce particle MCMC (PMCMC) methods that combine MCMC and SMC. One such PMCMC sampler is the particle Gibbs sampler that uses a particular conditional SMC update. This update is similar to the usual SMC approximation, but is conditioned on a prespecified reference trajectory $\boldsymbol{\theta}_{0:T}^*$ that is ensured to survive all resampling steps. Andrieu et al. (2010) show that conditioning on the reference trajectory makes the update a valid Markov kernel that leaves the conditional posterior $p(\boldsymbol{\theta}_{0:T}|y_{1:T}, \cdot)$ invariant, and can therefore be used in a Gibbs sampling step.

The particle Gibbs sampler can mix poorly due to path degeneracy in the underlying SMC sampler. The Particle Gibbs with Ancestor Sampling (PGAS) algorithm in Lindsten et al. (2014) improves the mixing by sampling the ancestor of the reference trajectory at each time t based on the ancestor weights

$$\tilde{w}_{t-1|T}^i \propto w_{t-1}^i f(\boldsymbol{\theta}_t^* | \boldsymbol{\theta}_{t-1}^i) \text{ for } i = 1, \dots, N, \quad (\text{S2.6})$$

in the special case of Markovian SSMS using the bootstrap filter. Lindsten et al. (2014) show that the ancestral sampling step does not compromise the validity of the Markov kernel, and can greatly improve mixing, even with few particles. The PGAS algorithm approximates the joint smoothing density with a single forward sweep, unlike other methods that often require explicit forward and backward sweeps (Lindsten and Schön, 2013). Algorithm S1 summarizes the PGAS sampler with the bootstrap filter, and we refer to Lindsten et al. (2014) for further details.

The initial proposal distribution $r_0(\boldsymbol{\theta}_0)$ is often taken as the prior $f_0(\boldsymbol{\theta}_0)$, but we find it useful for faster convergence to instead use the smoothing posterior at $t = 0$ from a short (500 draws) preliminary run of the approximate FFBSx described in the main article.

The PGAS algorithm can suffer from particle degeneracy in near-degenerate models (Lindsten et al., 2015), for example when the innovations in the transition model have close to zero variance for some t . A potential solution is to rejuvenate both the ancestors and the reference trajectory itself; see Lindsten et al. (2015) in the context of PGAS. However, we find that these modifications require careful adjustments to suit our specific model, indicating that further research is needed to adapt them effectively. We instead develop an approximate sampling step that replaces the Kalman filter in the FFBS sampler with the extended Kalman filter (EKF), as explained in our article.

Algorithm S1: PGAS Markov kernel for $p(\boldsymbol{\theta}_{0:T}|y_{1:T})$

Input: data $y_{1:T}$, reference trajectory $\boldsymbol{\theta}_{0:T}^*$, number of particles N , initial proposal distribution $q_0(\boldsymbol{\theta}_0)$ and resampling threshold ESS_{\min} .

```
\\ t = 0
 $\boldsymbol{\theta}_0^i \sim q_0(\boldsymbol{\theta}_0)$  for  $i = 1, \dots, N - 1$ 
 $\boldsymbol{\theta}_0^N = \boldsymbol{\theta}_0^*$ 
 $w_0^i \propto \frac{f_0(\boldsymbol{\theta}_0^i)}{q_0(\boldsymbol{\theta}_0^i)}$  for  $i = 1, \dots, N$ 
for  $t = 1$  to  $T$  do
  \\ resample
  if  $\text{ESS}_{t-1} < \text{ESS}_{\min}$  then
    draw  $a_t^i$  with  $P(a_t^i = j) \propto w_{t-1}^j$  for  $i = 1, \dots, N - 1$ 
    \\ sample the ancestor of reference particle
    draw  $a_t^N$  with  $P(a_t^N = j) \propto w_{t-1}^j f(\boldsymbol{\theta}_t^* | \boldsymbol{\theta}_{t-1}^j)$ 
    set  $w_{t-1}^i = \frac{1}{N}$  for  $i = 1, \dots, N$ 
  else
    | set  $a_t^i = i$  for  $i = 1, \dots, N$ 
  end

  \\ propagate the particles forward one step
  draw  $\boldsymbol{\theta}_t^i \sim f(\boldsymbol{\theta}_t^i | \boldsymbol{\theta}_{t-1}^{a_t^i})$  for  $i = 1, \dots, N - 1$ 
  set  $\boldsymbol{\theta}_t^N = \boldsymbol{\theta}_t^*$ 
  set  $\boldsymbol{\theta}_{1:t}^i = \{\boldsymbol{\theta}_{1:t-1}^{a_t^i}, \boldsymbol{\theta}_t^i\}$  for  $i = 1, \dots, N$ 

  \\ compute the importance weights
   $w_t^i \propto w_{t-1}^i g(y_t | \boldsymbol{\theta}_t^i)$  for  $i = 1, \dots, N$ 
end

Draw  $J$  with  $P(J = i) \propto w_T^i$ 
return  $\boldsymbol{\theta}_{0:T}^J$ 
```

S3 Gibbs sampling updating steps

This section describes the updating steps for the parameters not covered in the main text. The updates are independent across parameters and will therefore be described for one parameter without subscript k .

S3.1 Updating κ

The full conditional posterior of each κ_k are independent and we will here give the distribution for a typical element κ of $\boldsymbol{\kappa}$ conditional on its log-volatility process, which we denote by the generic $h_{0:T}$. The relevant part of the model in (2.5) for updating one of the κ parameters is

$$h_t = \mu + \kappa(h_{t-1} - \mu) + \eta_t, \quad \eta_t \stackrel{\text{iid}}{\sim} Z(1/2, 1/2, 0, 1), \text{ for } t = 1, \dots, T, \quad (\text{S3.1})$$

with initial condition $h_0 = \mu + \eta_0$ and $\eta_0 \sim Z(1/2, 1/2, 0, 1)$. Kowal et al. (2019) show that the model can be augmented with Polya-Gamma variables $\xi_{0:T}$ to become a conditionally Gaussian model

$$h_t = \mu + \kappa(h_{t-1} - \mu) + \eta_t \quad (\text{S3.2})$$

$$\eta_t | \xi_t \stackrel{\text{iid}}{\sim} N(0, \xi_t^{-1}) \quad (\text{S3.3})$$

$$\xi_t \stackrel{\text{iid}}{\sim} \text{PG}(1, 0), \quad (\text{S3.4})$$

Conditioning on the Polya-Gamma variables $\xi_{0:T}$, the parameter κ is the regression coefficient in a heteroscedastic Gaussian regression model. Multiplying both sides of (S3.2) by $\xi_t^{1/2}$ makes the model homoscedastic and a standard derivation for Bayesian linear regression shows that the full conditional posterior is

$$\kappa | \mu, \xi_{0:T}, h_{0:T} \sim TN(\kappa_T, \psi_T^2, -1, 1) \quad (\text{S3.5})$$

where $\psi_T^{-2} = \tilde{\mathbf{h}}_{-1}^\top \tilde{\mathbf{h}}_{-1} + \psi_0^{-2}$, $\kappa_T = w\hat{\kappa} + (1-w)\kappa_0$, $\hat{\kappa} = (\tilde{\mathbf{h}}_{-1}^\top \tilde{\mathbf{h}}_{-1})^{-1} \tilde{\mathbf{h}}_{-1}^\top \tilde{\mathbf{h}}$, $w = \frac{\tilde{\mathbf{h}}_{-1}^\top \tilde{\mathbf{h}}_{-1}}{\tilde{\mathbf{h}}_{-1}^\top \tilde{\mathbf{h}}_{-1} + \psi_0^{-2}}$, using the notation $\tilde{\mathbf{h}} = (\tilde{h}_1, \dots, \tilde{h}_T)^\top$ and $\tilde{\mathbf{h}}_{-1} = (\tilde{h}_0, \dots, \tilde{h}_{T-1})^\top$.

S3.2 Updating μ

The full conditional posteriors for the elements in $\boldsymbol{\mu}$ are independent and we will describe the updating step for one such generic element μ . We can rewrite the model in (S3.2)-(S3.4) as

$$z_t = \mu + \tilde{\eta}_t \quad (\text{S3.6})$$

where

$$z_t = \frac{h_t - \kappa h_{t-1}}{1 - \kappa}, \quad (\text{S3.7})$$

$$\tilde{\eta}_t = \eta_t / (1 - \kappa) \sim N\left(0, \tilde{\xi}_t^{-1}\right) \quad (\text{S3.8})$$

with $\tilde{\xi}_t = (1 - \kappa)^2 \xi_t$ and $z_0 = h_0 = \mu + \eta_0$ with $\eta_0 \sim N(0, \xi_0^{-1})$. This shows that μ is the mean of the transformed data z_t . A standard derivation of the posterior of a mean in a Gaussian model with known heteroscedastic variances shows that

$$\mu | \kappa, \xi_{0:T}, h_{0:T} \sim N(\mu_T, \sigma_T^2), \quad (\text{S3.9})$$

where $\sigma_T^{-2} = \sum_{t=0}^T \tilde{\xi}_t + \sigma_0^{-2}$ and $\mu_T = v\hat{\mu} + (1 - v)\mu_0$ with

$$v = \frac{\sum_{t=0}^T \tilde{\xi}_t}{\sum_{t=0}^T \tilde{\xi}_t + \sigma_0^{-2}}. \quad (\text{S3.10})$$

S3.3 Updating the $\log \chi_1^2$ mixture allocation $\mathbf{a}_{1:T}$

This is a standard step based on the 10-component mixture in Omori et al. (2007); see Kowal et al. (2019) for details.

S3.4 Updating $\xi_{1:T}$

The updating of the Polya-Gamma variables is identical to the update in Kowal et al. (2019).

S3.5 Updating the observational noise variance

For the static variance case we use the conjugate prior $\sigma^2 \sim \text{Scale-Inv-}\chi^2(v_0, s_0^2)$. The posterior distribution is $\text{Scale-Inv-}\chi^2(v_T, s_T^2)$, with $v_T = v_0 + T$ and $s_T^2 = (v_0 s_0^2 + \sum_{i=1}^T \hat{\epsilon}_i^2) / (v_0 + T)$.

In the time-varying error variance case, we follow Kowal et al. (2019) and use a stochastic volatility (SV) model with the updating step in Kastner and Frühwirth-Schnatter (2014), similarly to the sampling of h_{kt} in Section 3.1.

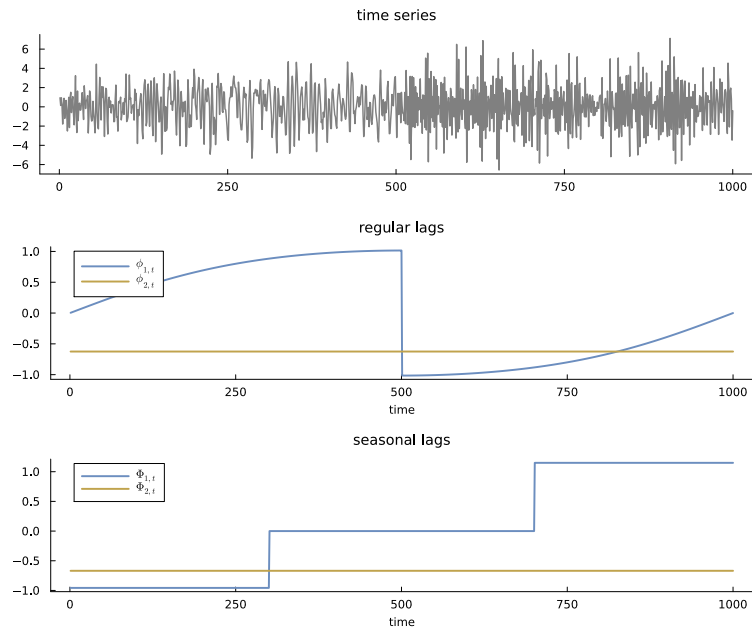


Figure S2: Experiment 1. A time series realization from the data generating process (top row), the evolution of the regular AR parameters (second row) and seasonal parameters (third row).

S4 Additional results from the simulation experiments

S4.1 Experiment 1

The top panel in Figure S2 illustrates a typical realization from the model in Experiment 1, with the middle and bottom panels showing the true regular ϕ_t and seasonal Φ_t AR coefficients mapped to the stability region. Figure S3 shows the time evolution of the eigenvalues of the companion matrix of the regular and seasonal AR coefficients.

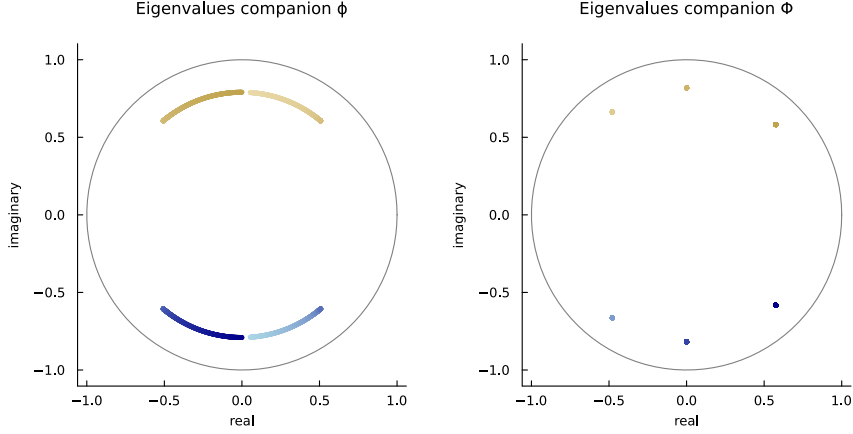


Figure S3: Experiment 1. Eigenvalues for the companion matrix of the regular and seasonal polynomials over time for the data generating process. The color scale for the eigenvalues represents time, with darker colors indicating later points in the time sequence.

	FFBSx-m			FFBSx-l			PGAS(100)		
	$\pi/4$	$\pi/2$	$3\pi/4$	$\pi/4$	$\pi/2$	$3\pi/4$	$\pi/4$	$\pi/2$	$3\pi/4$
$t = 100$	377	330	460	506	475	533	38	35	41
$t = 400$	418	454	436	548	620	595	167	216	179
$t = 800$	375	412	361	418	534	474	324	412	348

Table S2: Experiment 1. Effective sample size (ESS) for estimating the spectral density for three algorithms. ESS for the spectral density is computed at three selected time points (rows) and at three selected frequencies (columns). The ESS is from an initial posterior sample of 10 000 draws thinned down to 1000 draws. An offset of 10^{-16} is used.

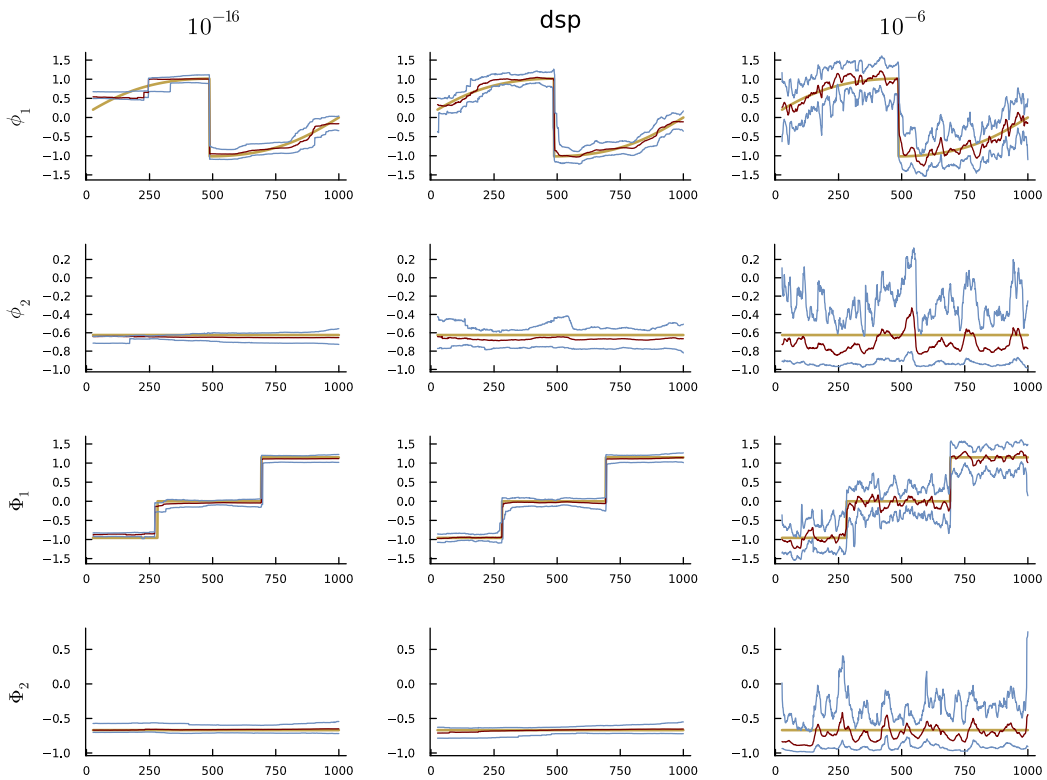


Figure S4: Experiment 1. Posterior median and 95% credible intervals from PGAS(100) from one run for the three different offsets in the log-volatility model for \mathbf{h}_t

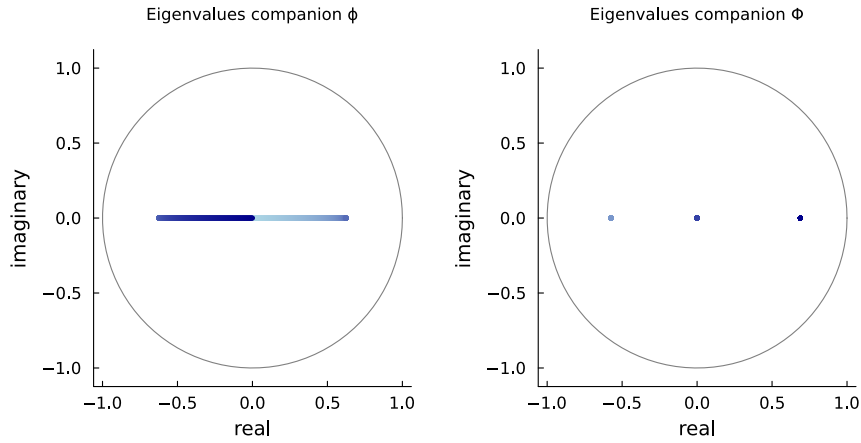


Figure S5: SAR(1,1). Eigenvalues for the companion matrix of the regular and seasonal polynomials over time for the data generating process. The color scale for the eigenvalues represents time, with darker colors indicating later points in the time sequence.

S4.2 Experiment 1 - one lag version

In this experiment, data is simulated from the following one-lag restricted version of the DGP in Experiment 1, a time-varying TVSAR(\mathbf{s}, \mathbf{p}) with $\mathbf{s} = (1, 12)$ and $\mathbf{p} = (1, 1)$,

$$(1 - \phi_{1t}L)(1 - \Phi_{1t}L^{12})y_t = \varepsilon_t, \quad (\text{S4.1})$$

where $\varepsilon_t \sim N(0, 1)$. The time evolution of the parameters are the same as for the first regular and seasonal lag in Experiment 1. Figure S5 shows the time evolution of the eigenvalues of the companion matrix of the regular and seasonal AR coefficients.

Figures S6 and S7 show that the PGAS convergence is much better than for the SAR(2,2) model in Experiment 1, already for an offset of 10^{-16} .

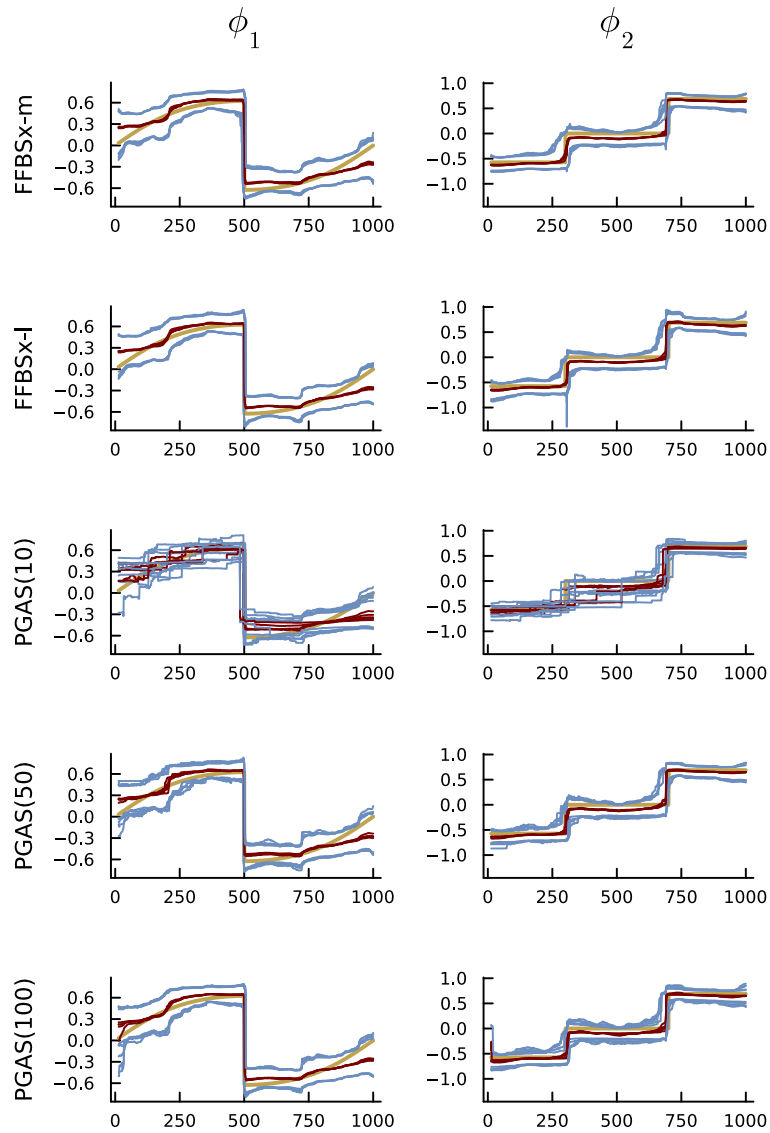


Figure S6: SAR(1,1). Assessing MCMC convergence of different sampling algorithms by re-estimating the model using five different initial values drawn from the prior of the global hyperparameters μ and κ . The red and blue lines are posterior medians and 95% equal tail credible bands over time for each of the five repeated runs. The beige line is the true parameter evolution given by (4.5) and (4.6).

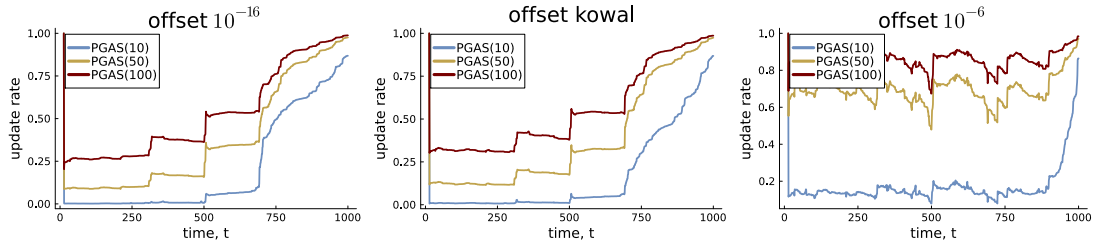


Figure S7: SAR(1,1). PGAS update rates for three different offsets in the log-volatility model for \mathbf{h}_t for different numbers of particles.

	FFBSx-m			FFBSx-l			PGAS(100)		
	$\pi/4$	$\pi/2$	$3\pi/4$	$\pi/4$	$\pi/2$	$3\pi/4$	$\pi/4$	$\pi/2$	$3\pi/4$
$t = 100$	498	514	482	593	606	587	226	237	215
$t = 400$	368	542	337	411	563	375	257	333	238
$t = 800$	483	597	505	496	767	536	412	620	457

Table S3: Experiment 2. Effective sample size (ESS) for estimating the spectral density for three algorithms. ESS for the spectral density is computed at three selected time points (rows) and at three selected frequencies (columns). The ESS is from an initial posterior sample of 10 000 draws thinned down to 1000 draws. An offset of 10^{-16} is used.

S4.3 Experiment 2

The top panel of Figure S8 shows a typical realization from the model in Experiment 2. The bottom panels of the figure show the time evolution of the true regular ϕ_t and seasonal Φ_t AR coefficients mapped to the stability region. Figure S9 shows the time evolution of the eigenvalues of the companion matrix of the regular and seasonal AR coefficients; the eigenvalues are slightly jittered smoothly to avoid a complete overlap. Table S3 display effective sample sizes for spectral density estimates for the different posterior algorithms for the TVSAR model. Figures S10-S13 give additional results for Experiment 2.

S4.4 Experiment 3

Figures S14-S16 give additional results for Experiment 3.

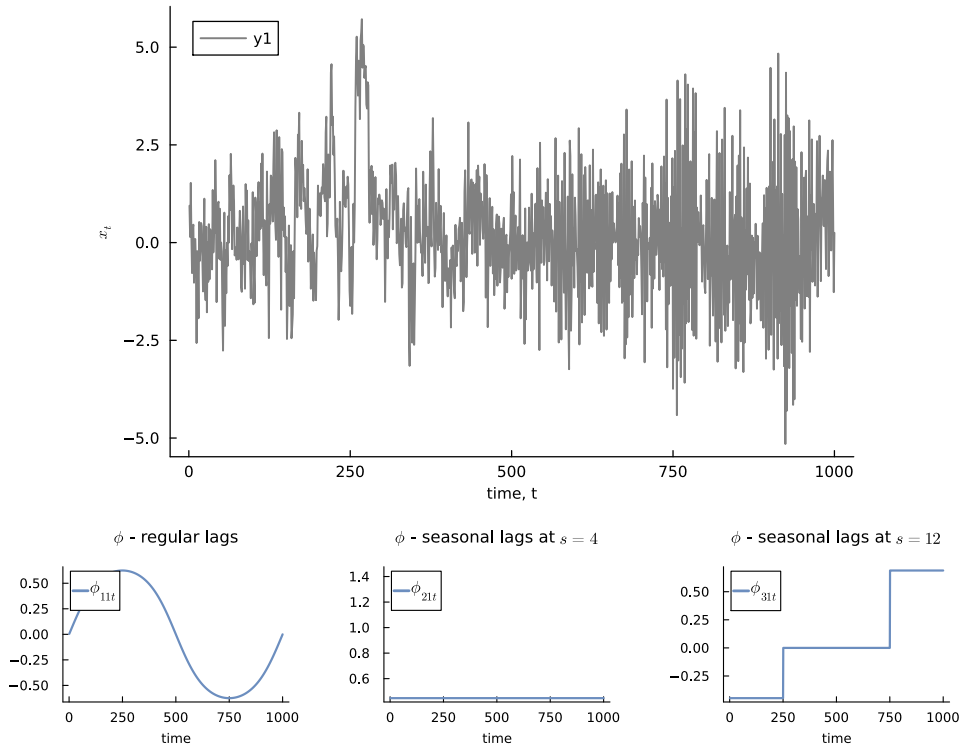


Figure S8: Experiment 2. A time series realization from the data generating process (top row), the evolution of the regular AR parameters (second row, left panel) and seasonal parameters (second row, middle and right panels).

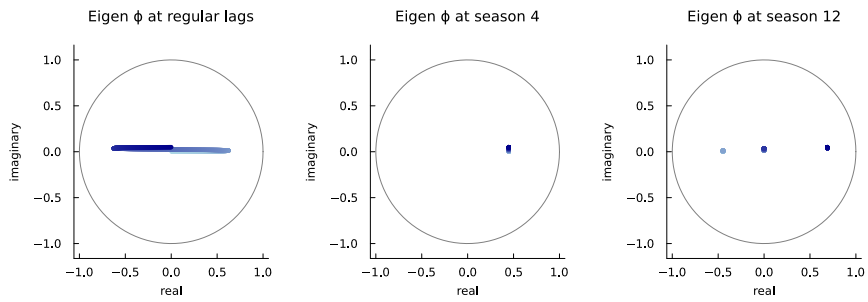


Figure S9: Experiment 2. Eigenvalues for the companion matrix of the regular and seasonal polynomials over time for the data generating process. The color scale for the eigenvalues represents time, with darker colors indicating later points in the time sequence.

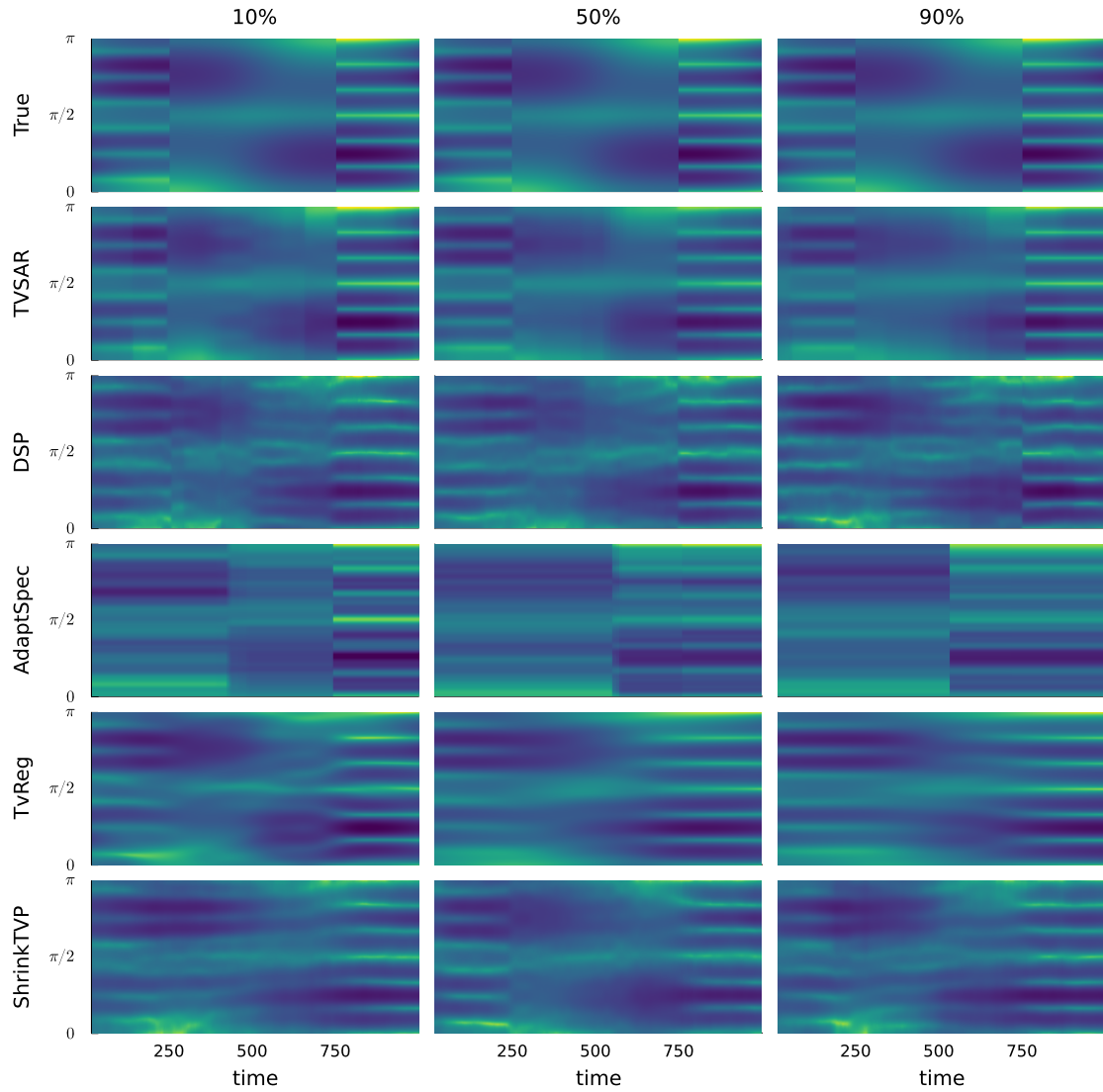


Figure S10: Experiment 2. Heat maps of the estimated spectrogram for the different methods. The columns correspond to different datasets chosen from the percentiles of each model's MSE distribution, to showcase the performance of each model when it performs well (10%), average (50%) and poorly (90%).

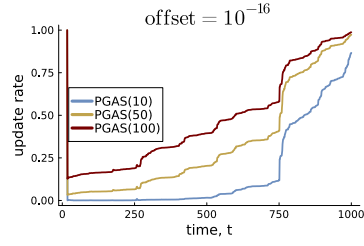


Figure S11: Experiment 2. PGAS update rates for the smallest offset 10^{-16} in the log-volatility model for \mathbf{h}_t for different numbers of particles.

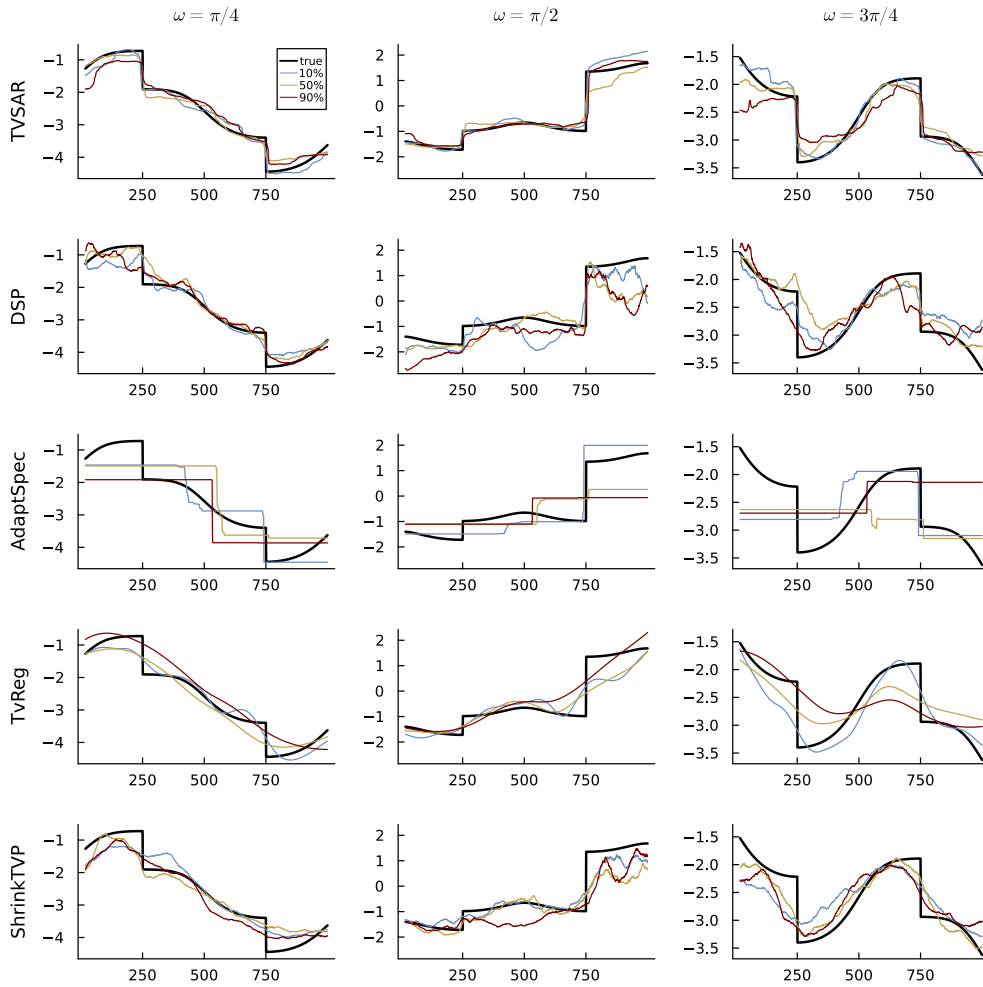


Figure S12: Experiment 2. Time evolution of the log spectral density at three different frequencies. The black line is the true spectral density and the three colored lines are the posterior median from three different datasets chosen from the MSE percentiles.

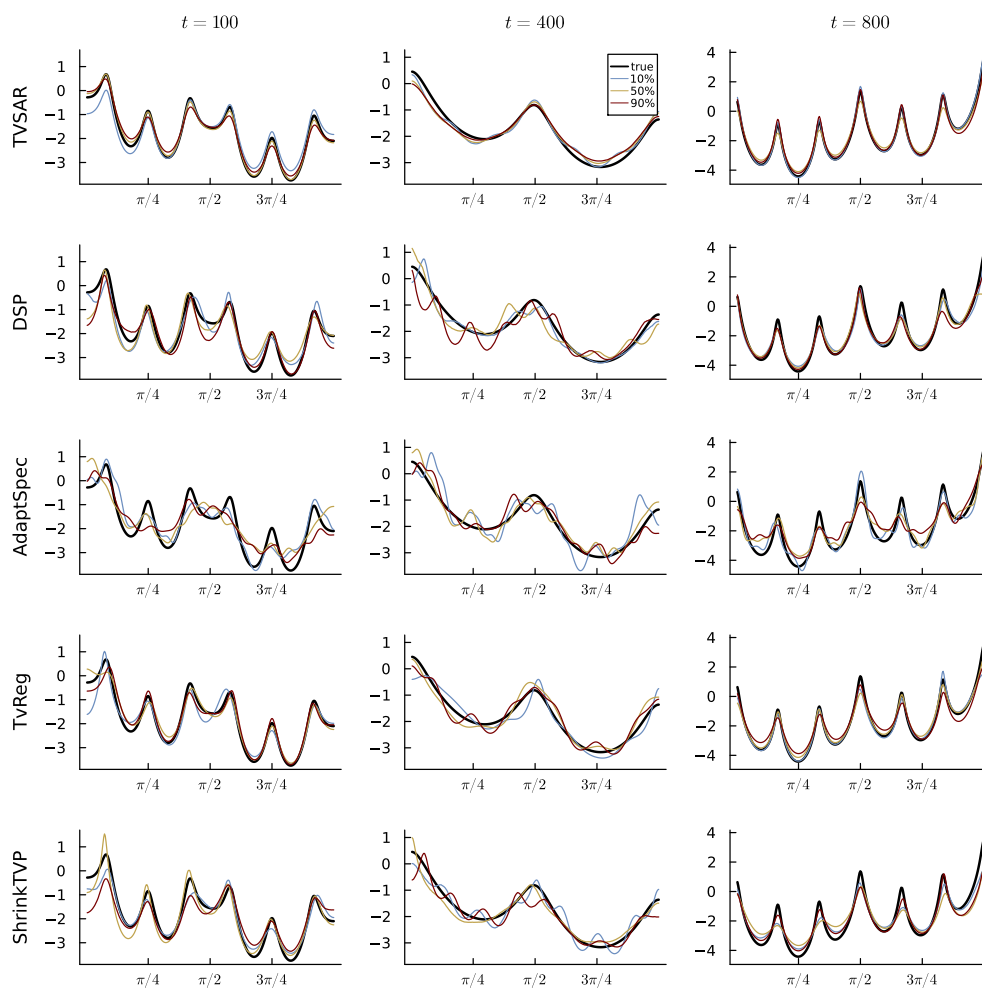


Figure S13: Experiment 2. Log spectral density at three different time points. The black line is the true spectral density and the three colored lines are the posterior median from three different datasets chosen from the MSE percentiles.

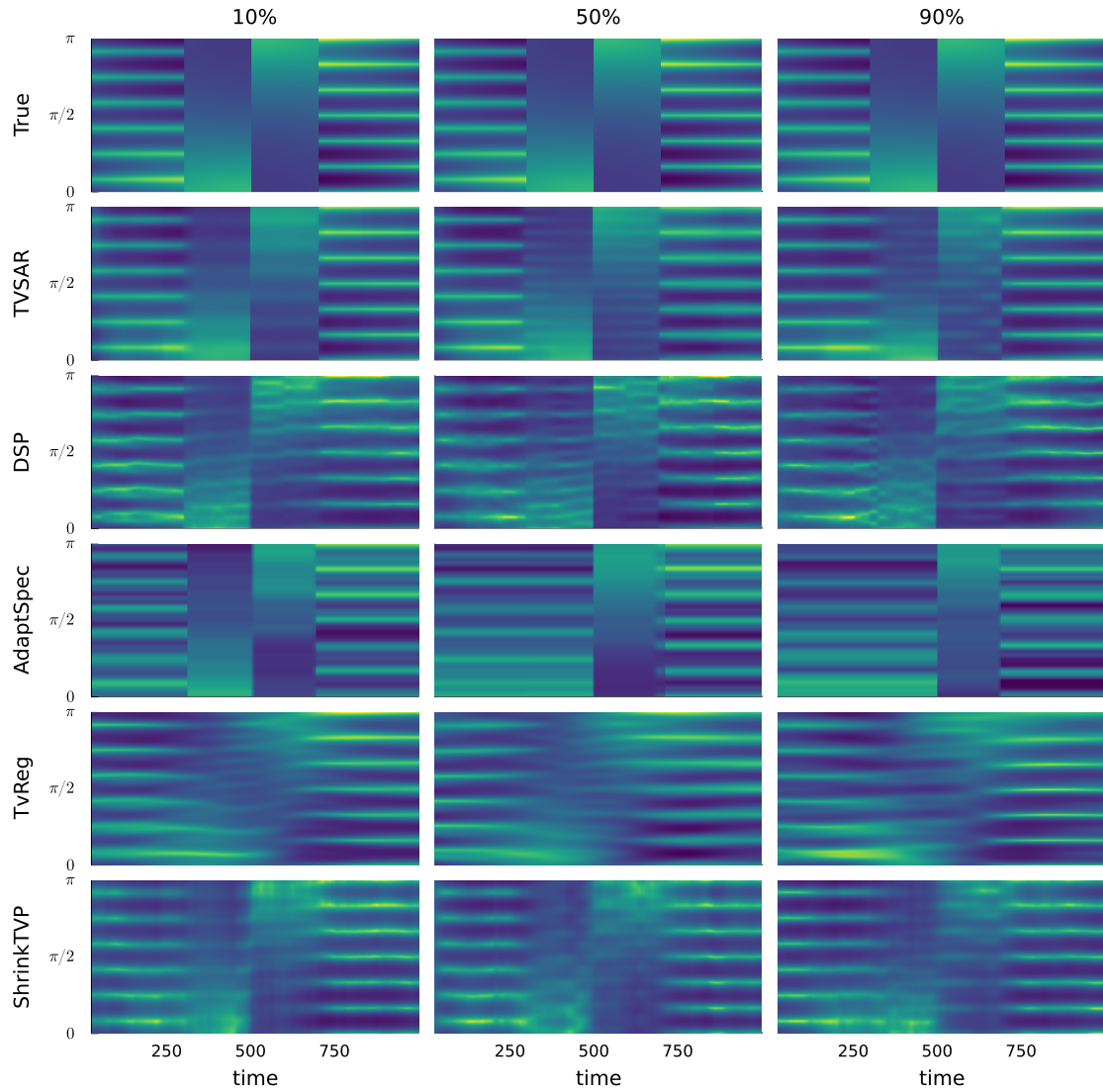


Figure S14: Experiment 3. Heatmaps of the estimated spectrogram for the different methods. The columns correspond to different datasets chosen from the percentiles of each model's MSE distribution, to showcase the performance of each model when it performs well (10%), average (50%) and poorly (90%).

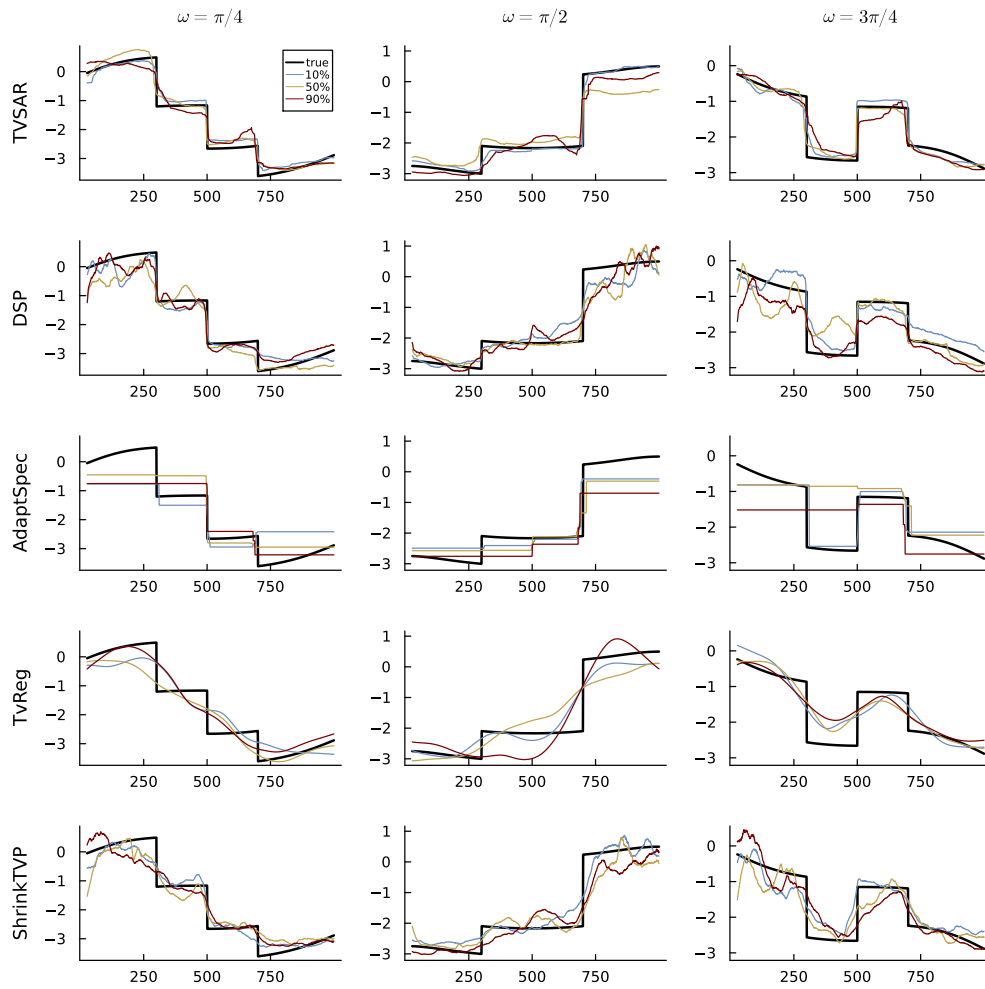


Figure S15: Experiment 3. Time evolution of the log spectral density at three different frequencies. The black line is the true spectral density and the three colored lines are the posterior median from three different datasets chosen from the MSE percentiles.

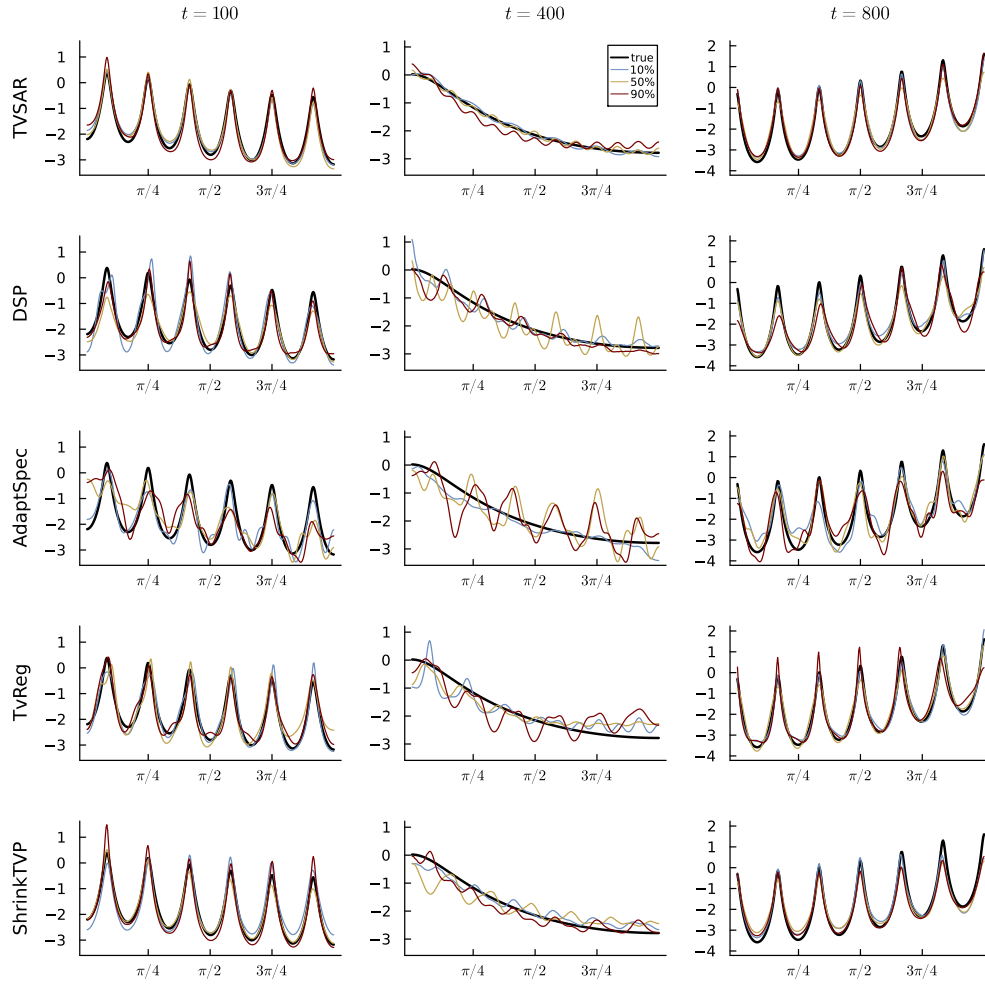


Figure S16: Experiment 3. Log spectral density at three different time points. The black line is the true spectral density and the three colored lines are the posterior median from three different datasets chosen from the MSE percentiles.

S5 Additional results - US industrial production

Figure S17 assesses the convergence of the FFBS-x algorithm on the US industrial production data by plotting the posterior medians and equal-tail 95% credible intervals from three different runs, each with different initial values. The initial values for the global parameters are set so that $\mu_k = \mu$ and $\kappa_k = \kappa$ for all k , with μ and κ drawn from their respective priors in each run of the algorithm.

Figure S18 plots the posterior median and equal-tail 95% credible bands from the PGAS algorithm with 100 particles for the US industrial production data.

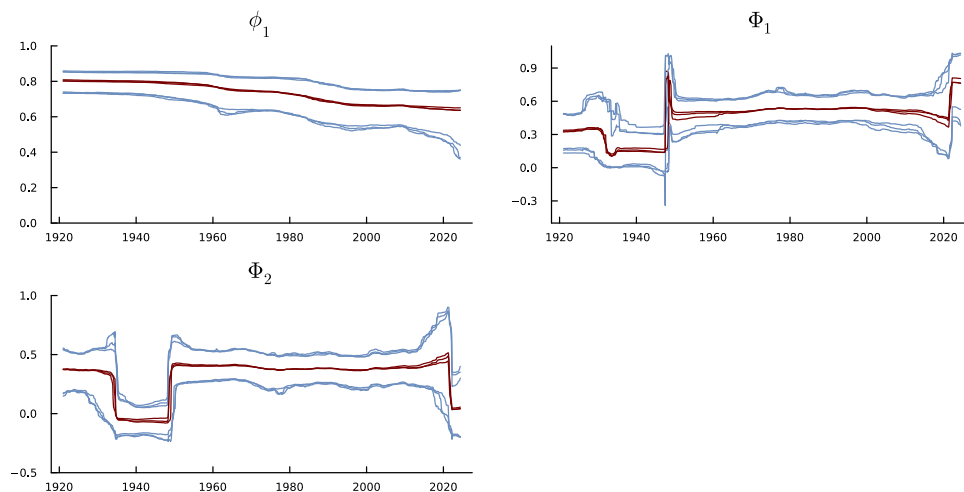


Figure S17: US industrial production. The posterior median and 95% credible intervals from the SAR(1,2) model with dynamic shrinkage prior and stochastic volatility, obtained with the FFBSx algorithm using an offset of 10^{-16} . The posterior median and 95% credible intervals are shown for three runs based on different initial values drawn from the prior.

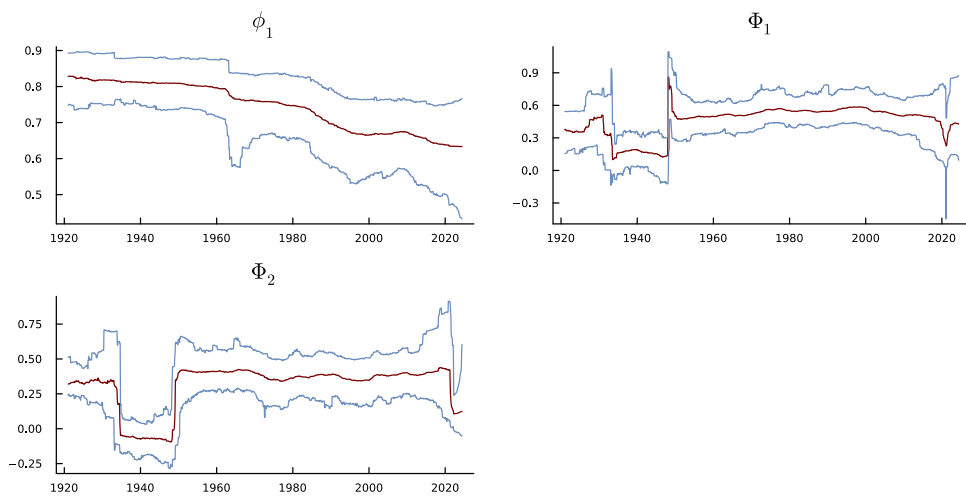


Figure S18: US industrial production. Posterior from SAR(1,2) model with stochastic volatility obtained with the PGAS algorithm with $N = 100$ particles using an offset of 10^{-16} .